

THE YOUNG AGE OF THE EXTREMELY METAL-DEFICIENT BLUE COMPACT DWARF GALAXY SBS 1415+437^{1,2}

Trinh X. Thuan

*Astronomy Department, University of Virginia, Charlottesville VA 22903
Electronic mail: txt@virginia.edu*

Yuri I. Izotov³

*Main Astronomical Observatory, Ukrainian National Academy of Sciences, Goloseevo, Kiev 252650, Ukraine
Electronic mail: izotov@mao.kiev.ua*

and

Craig B. Foltz

*Multiple Mirror Telescope Observatory, University of Arizona, Tucson, AZ 85721
Electronic mail: cfoltz@as.arizona.edu*

ABSTRACT

We use Multiple Mirror Telescope (MMT) spectrophotometry and *Hubble Space Telescope* (*HST*) Faint Object Spectrograph (FOS) spectra and Wide Field and Planetary Camera 2 (WFPC2) *V* and *I* images to study the properties and evolutionary status of the nearby ($D = 11.4$ Mpc) extremely metal-deficient blue compact dwarf (BCD) galaxy SBS 1415+437 \equiv CG 389. The oxygen abundance in the galaxy is $12 + \log(\text{O}/\text{H}) = 7.60 \pm 0.01$ or $Z_{\odot}/21$.

The helium mass fraction in SBS 1415+437 is $Y = 0.246 \pm 0.004$ which agrees with the primordial helium abundance determined by Izotov & Thuan using a much larger sample of BCDs. The α -elements-to-oxygen abundance ratios (Ne/O, S/O, Ar/O) are in very good agreement with the mean values for other metal-deficient BCDs and are consistent with the scenario that these elements are made in massive stars. The Fe/O abundance ratio is ~ 2 times smaller than the solar ratio. The Si/O ratio is close to the solar value, implying that silicon is not significantly depleted into dust grains. The values of the N/O and C/O ratios imply that intermediate-mass stars have not had time to evolve in SBS 1415+437 and release their nucleosynthesis products and that both N and C in the BCD have been made by massive stars only. This sets an upper limit of ~ 100 Myr on the age of SBS 1415+437.

¹Based on observations obtained with the NASA/ESA *Hubble Space Telescope* through the Space Telescope Science Institute, which is operated by AURA, Inc. under NASA contract NAS5-26555.

²Ground-based spectroscopic observations presented herein were obtained with the Multiple Mirror Telescope, a facility operated jointly by the Smithsonian Institution and the University of Arizona.

³Visiting astronomer, National Optical Astronomical Observatories.

The V and I surface brightness profiles of SBS 1415+437 are well fitted by exponentials implying that the galaxy is a disk-like system. The velocity distribution derived from the $H\alpha$ and [O III] $\lambda 5007$ emission lines indicates a solid-body rotation with a rotational velocity of 80 km s^{-1} . The dynamical mass is ~ 13 times larger than the gas mass, implying that most of the mass in SBS 1415+437 is in the form of dark matter. The $(V - I)$ color of the low-surface-brightness component of the galaxy is blue ($\lesssim 0.4 \text{ mag}$) indicative of a very young underlying stellar population. The $(V - I) - I$ color-magnitude diagrams of the resolved stellar populations in different regions of SBS 1415+437 suggest propagating star formation from the NE side of the galaxy to the SW.

All regions in SBS 1415+437 possess very blue spectral energy distributions (SED). By comparing the observed SEDs to theoretical SEDs which include both stellar and gaseous emission, we find that the ages of the stellar populations in SBS 1415+437 to range from a few Myr to 100 Myr. Thus chemical abundances, color profiles and spectral energy distributions all say that SBS 1415+437 is a truly young galaxy which did not start to make stars until ~ 100 Myr ago.

Subject headings: galaxies: abundances — galaxies: irregular — galaxies: photometry — galaxies: evolution — galaxies: formation — galaxies: ISM — H II regions — ISM: abundances

1. INTRODUCTION

The evolutionary status of low-metallicity blue compact dwarf (BCD) galaxies has been debated for decades, ever since the pioneering paper by Searle, Sargent & Bagnuolo (1973). Are BCDs truly young systems where star formation is occurring for the first time or are they old galaxies with an old underlying stellar population on which the current starburst is superposed? An argument in favor of their youth would be their heavy element abundance which ranges between $Z_{\odot}/50$ and $Z_{\odot}/3$, placing them among the least chemically evolved galaxies in the universe. On the other hand, subsequent surface photometric studies have shown that the majority of BCDs are not young and that they have experienced star formation episodes in the past. Loose & Thuan (1985) found that $\sim 95\%$ BCDs in their sample exhibit an underlying red extended low surface brightness component, on which are superposed the high surface brightness star-forming regions. Later CCD surveys of BCDs have confirmed and strengthened that initial result (Kunth, Maurogordato & Vigroux 1988; Papaderos et al. 1996; Telles & Terlevich 1997).

However, there are at least two known BCDs with extremely young stellar populations. They are the two most-metal deficient galaxies known, I Zw 18 ($Z_{\odot}/50$) and SBS 0335–052 ($Z_{\odot}/41$). *Hubble Space Telescope* (*HST*) imaging to $V \sim 26$ of I Zw 18 by Hunter & Thronson (1995) suggests that the stellar population is dominated by young stars and that the colors of the underlying diffuse component are consistent with those from a sea of unresolved B or early A stars, with no evidence for stars older than $\sim 10^7$ yr. The BCD SBS 0335–052 was first shown by Izotov et al. (1990) to possess an extraordinarily low metallicity. *HST* V and I imaging of this galaxy (Thuan, Izotov & Lipovetsky 1997) show blue ($V - I$) colors not only in the region of current star formation, but also in the extended, low-surface-brightness envelope some 4 kpc in diameter. Izotov et al. (1997a) and Papaderos et al. (1998) have shown that $\sim 1/3$ of the emission from the underlying component, with color ($V - I$) = 0.0 - 0.2, comes from ionized gas while the remaining 2/3 come from young stars not older than $\sim 10^8$ yr. Another piece of evidence in favor of the youth of SBS 0335–052 is provided by Thuan & Izotov (1997). From *HST* UV spectrophotometry, they found that SBS 0335–052 is a damped Ly α system with an extremely high neutral hydrogen column

density $N(\text{H I}) = 7 \times 10^{21} \text{ cm}^{-2}$, suggesting a large amount of neutral gas around the galaxy. In fact, a Very Large Array (VLA) map of SBS 0335–052 does show the presence of a large extended H I cloud, 64 kpc by 24 kpc in size, and with mass $\sim 10^9 M_{\odot}$, some two orders of magnitude larger than the observed stellar mass (Pustilnik et al. 1999). There are two prominent, slightly-resolved H I peaks separated by 22 kpc, one of which is associated with SBS 0335–052, and the other with a fainter dwarf galaxy, which is even slightly more metal-deficient ($Z_{\odot}/50$, Lipovetsky et al. 1999a). Thuan & Izotov (1997) have argued that the H I envelope may be truly primordial, unpolluted by heavy elements.

The above observational evidence suggests that there may be truly young dwarf galaxies in the local universe which started to make stars for the first time less than about 100 Myr ago. The study of such young galaxies is important not only for their intrinsic interest, but also for understanding galaxy formation at high redshift. Their proximity allows studies of their structure, metal content and stellar populations with a sensitivity, precision and spatial resolution that faint, small and distant high-redshift galaxies do not allow. We have therefore started a search for other young galaxies among the most metal-deficient BCDs known. In that search, we were guided by the work of Izotov & Thuan (1999) who have argued that chemical abundances in BCDs can put constraints on their age. Their conclusion, based on the behavior of the C/O and N/O ratios as a function of O abundance, is that all galaxies with $12 + \log(\text{O}/\text{H}) \lesssim 7.6$ ($Z_{\odot}/20$) began to form stars less than ~ 100 Myr ago.

A most attractive candidate is the BCD SBS 1415 + 437 \equiv CG 387, which possesses a metallicity of only $Z_{\odot}/21$ and which is near enough ($v = 607 \text{ km s}^{-1}$) to allow resolution into stars. Its general characteristics are shown in Table 1. At the distance of 11.4 Mpc adopted for SBS 1415+437, $1''$ corresponds to 55 pc. We report here new Multiple Mirror Telescope (MMT) spectroscopy, *HST* Faint Object Spectrograph (FOS) UV and optical spectroscopy and Wide Field and Planetary Camera 2 (WFPC2) V and I imaging of the BCD. We then use these data to discuss the evolutionary status of this nearby dwarf galaxy. We describe the MMT and *HST* observations in §2. The heavy element and helium abundances are derived in §3. The morphology and kinematics of the ionized gas are discussed in §4. In §5 we discuss the stellar populations in SBS 1415+437. We summarize

our findings in §6.

2. OBSERVATIONS AND DATA REDUCTION

2.1. MMT optical spectroscopy

Spectrophotometric observations of SBS 1415+437 with a signal-to-noise ratio $S/N = 30$ in the continuum were obtained with the Multiple Mirror Telescope (MMT) on the night of 1997 May 1. The observations were made with the Blue Channel of the MMT Spectrograph using a highly-optimized Loral 3072×1024 CCD detector. A $1''.5 \times 180''$ slit was used along with a 500 g/mm grating in first order and an L-38 second-order blocking filter. This gives a spatial scale along the slit of $0.3 \text{ arcsec pixel}^{-1}$, a scale perpendicular to the slit of $1.9 \text{ \AA pixel}^{-1}$, a spectral range of 3600–7300 Å and a spectral resolution of $\sim 7 \text{ \AA FWHM}$. For these observations, CCD rows were binned by a factor of 2, yielding a final spatial sampling of $0.6 \text{ arcsec pixel}^{-1}$. The observations cover in a single frame the full spectral range, with all the lines of interest from [O II] $\lambda 3727$ to [O II] $\lambda 7330$. Furthermore, they have sufficient spectral resolution to separate [O III] $\lambda 4363$ from nearby $H\gamma$ and to distinguish between narrow nebular and broad Wolf-Rayet emission lines. The total exposure time was 90 minutes and was broken up into 3 subexposures, 30 minutes each, to allow for more effective cosmic-ray removal. All exposures were taken at small airmasses ($\lesssim 1.05$), so no correction was made for atmospheric dispersion. The seeing during the observations was $1''$ FWHM. The slit was oriented in the direction with position angle 22° , along the major axis of the galaxy. The spectrophotometric standard star HZ 44 was observed for flux calibration. Spectra of He–Ne–Ar comparison lamps were obtained before and after each observation to provide wavelength calibration.

Data reduction of the spectral observations was carried out at the NOAO headquarters in Tucson using the IRAF⁴ software package. This included bias subtraction, cosmic-ray removal and flat-field correction using exposures of a quartz incandescent lamp. Wavelength calibration was performed for the 2-dimensional spectrum by constructing dispersion

curves for successive 30 pixels wide regions along the slit, using the comparison spectrum. The amplitude of the scatter of the points around each dispersion curve is $\lesssim 0.1 \text{ \AA}$. We then correct the spectrum for distortion and tilt and obtain the wavelength-calibrated two-dimensional spectrum by using the IRAF routine TRANSFORM. The accuracy of the wavelength calibration along the slit was checked by measuring the wavelength of the bright night sky line [O I] $\lambda 5577$. We found the dispersion of the measured wavelengths to be $\sim 0.06 \text{ \AA}$, equivalent to velocity errors of $\sim 3 \text{ km s}^{-1}$.

After night sky background subtraction, and correcting for atmospheric extinction, each frame was calibrated to absolute fluxes. To derive the sensitivity curve, we have fitted the observed spectral energy distribution of the bright hot white dwarf standard star HZ 44 with a high-order polynomial. Because the spectrum of HZ 44 has only a small number of relatively weak absorption features, its spectral energy distribution is known with the very good precision of $\sim 1 \%$ (Oke 1990). We were thus able to derive a sensitivity curve with a precision of $\sim 1 \%$ over the whole optical range, except in the region blueward of [O II] $\lambda 3727$ where the sensitivity drops precipitously. One-dimensional spectra were extracted by summing, without weighting, of different numbers of rows along the slit depending on the exact region of interest. The spectrum of SBS 1415+437 in the region $3600 \text{ \AA} \leq \lambda \leq 7500 \text{ \AA}$ for the aperture $1''.5 \times 5''$ is shown in Figure 1. The continuum was fitted after removal of the emission lines, and line intensities were measured by fitting Gaussians to the profiles.

We have adopted an iterative procedure to derive both the extinction coefficient $C(H\beta)$ and the absorption equivalent width for the hydrogen lines simultaneously from the equation (Izotov, Thuan & Lipovetsky 1994, 1997, hereafter respectively ITL94 and ITL97):

$$\frac{I(\lambda)}{I(H\beta)} = \frac{EW_e(\lambda) + EW_a(\lambda)}{EW_e(\lambda)} \frac{EW_e(H\beta)}{EW_e(H\beta) + EW_a(H\beta)} \times \frac{F(\lambda)}{F(H\beta)} 10^{[C(H\beta)f(\lambda)]}, \quad (1)$$

where $I(\lambda)$ is the intrinsic line flux and $F(\lambda)$ is the observed line flux corrected for atmospheric extinction. $EW_e(\lambda)$ and $EW_a(\lambda)$ are the equivalent widths of the observed emission line and the underlying absorption line, respectively, and $f(\lambda)$ is the reddening

⁴IRAF: the Image Reduction and Analysis Facility is distributed by the National Optical Astronomy Observatories, which is operated by the Association of Universities for Research in Astronomy, Inc. (AURA) under cooperative agreement with the National Science Foundation (NSF).

function, normalized at $H\beta$, which we take from Whitford (1958).

We use the theoretical ratios from Brocklehurst (1971) at the electron temperature estimated from the observed $[O\ III](\lambda 4959 + \lambda 5007)/\lambda 4363$ ratio for the intrinsic hydrogen line intensity ratios. For lines other than hydrogen $EW_a(\lambda) = 0$, so Eq. (1) reduces to

$$\frac{I(\lambda)}{I(H\beta)} = \frac{F(\lambda)}{F(H\beta)} 10^{[C(H\beta)f(\lambda)]}. \quad (2)$$

The observed and corrected line intensities, extinction coefficient, and equivalent widths of the stellar hydrogen absorption lines are given in Table 2 along with the uncorrected $H\beta$ flux and $H\beta$ equivalent width for the brightest part of SBS 1415+437. We give the line intensities for two different apertures, a large one ($1''.5 \times 5''$) and a small one ($1''.5 \times 0''.6$). While the spectrum associated with the larger aperture has a higher signal-to-noise ratio, the one associated with the smaller aperture is useful for comparing with the *Hubble Space Telescope* (*HST*) Faint Object Spectrograph (FOS) spectra which were obtained with a $0''.86$ circular aperture.

2.2. *HST* observations

2.2.1. Imaging

We obtained images of SBS 1415+437 on 1995 April 17 during cycle 4, after the refurbishment mission, with the *HST* Wide Field and Planetary Camera 2 (WFPC2) in filters F569W and F791W, which we will refer to as V and I throughout the paper. Two exposures of equal duration were obtained in each filter to permit identification and removal of cosmic rays. The total exposure time was 1800s in V and 4400s in I . The scale of the WFPC2 is $0''.102$ per pixel.

Preliminary processing of the raw images including corrections for flat-fielding was done at the Space Telescope Science Institute through the standard pipeline. Subsequent reductions were carried out at the University of Virginia using IRAF and STSDAS⁵. Cosmic rays were removed and the images in each filter were combined. We found that all exposures in a given filter coregistered to better than ~ 0.2 pixels. The transformation of instrumental magnitudes to the Johnson-Cousins $UBVRI$ photometric system

as defined by Landolt (1992) was performed according to the prescriptions of Holtzman et al. (1995b).

The resulting measured brightness of the sky background is 23.0 mag arcsec⁻² in V and 22.2 mag arcsec⁻² in I .

2.2.2. Spectrophotometry

We also obtained ultraviolet and optical spectra of SBS 1415+437 with the Faint Object Spectrograph (FOS) during cycle 4 on 1995 January 24. The UV spectrum was obtained with grating G190H and an integration time of 1600s and covers the wavelength range $\lambda 1572 - 2312 \text{ \AA}$. The optical spectra were obtained with grating G400H and an exposure time of 960s in the blue range ($\lambda 3235 - 4781 \text{ \AA}$) and with grating G570H and an exposure time of 1260s in the red range ($\lambda 4569 - 6818 \text{ \AA}$). The spectra were taken consecutively in time with the $0''.86$ circular aperture (aperture B-3) giving a spectral resolution of $\sim 3 \text{ \AA}$ for the UV spectrum, $\sim 6 \text{ \AA}$ for the blue spectrum and $\sim 9 \text{ \AA}$ for the red one.

The spectra were processed through the standard *HST* pipeline reductions, with corrections for flat-fielding, wavelength determination, instrumental background subtraction and photometric calibration. The instrumental and sky backgrounds were negligible for our observations. The FOS spectra are shown in Fig. 2 where all emission lines are marked. Note that in the UV spectrum, the Si III] $\lambda 1892$ emission line is not present. Instead, there is an absorption feature at the location of the line. By examining the count rates vs diodes in the uncalibrated spectrum, we have determined the absorption feature to be caused by several bad diodes. Thus for our analysis, we shall assume that the Si III] $\lambda 1892$ emission line is emitted in the H II region with a flux 0.67 times that of Si III] $\lambda 1883$, as expected in the low density limit from the statistical weight ratio of the Si²⁺ 3P_2 and 3P_1 levels.

The observed emission line fluxes in the FOS spectra are dereddened according to Eq. (1) and (2). In the optical range we again use the reddening function from Whitford (1958), and in the UV range the Small Magellanic Cloud reddening curve as parameterized by Prévot et al. (1984).

The observed and corrected line fluxes of the *HST* spectra are shown in Table 2 together with those from the ground-based optical observations. The errors given include statistical uncertainties plus a 1 % error in the flux calibration. They have been propagated

⁵STSDAS: the Space Telescope Science Data Analysis System.

to derive element abundances and their errors. The extinction coefficients $C(H\beta)$ derived from the MMT small aperture spectrum and the *HST* spectrum are very similar. They are very small, being 0.025 and 0.020 dex, respectively.

3. HEAVY ELEMENTS AND HELIUM ABUNDANCES

Since SBS 1415+437 has been observed over a wide spectral range with a high signal-to-noise ratio, reliable heavy element abundances of the ionized gas can be derived. The heavy element abundance ratios allow to place constraints on stellar nucleosynthesis processes in a very metal-deficient environment and on the chemical evolution of the BCD. Of special interest is the determination of the helium abundance which should approximate well the primordial value as SBS 1415+437 is one of the most metal-deficient BCDs known.

3.1. Abundance determination

To derive element abundances from the optical line intensities, we follow the procedures detailed in ITL94 and ITL97. It is known that the electron temperature, T_e , is different in high- and low-ionization zones of H II regions (Stasińska 1990). We have chosen to determine $T_e(\text{O III})$ from the $[\text{O III}] \lambda 4363/(\lambda 4959 + \lambda 5007)$ ratio using the five-level atom model (Aller 1984) and $N_e(\text{S II})$ from the $[\text{S II}] \lambda 6717/\lambda 6731$ ratio. We adopt $T_e(\text{O III})$ for the derivation of He^+ , He^{2+} , O^{2+} , Ne^{2+} and Ar^{3+} ionic abundances. To derive the electron temperature for the O^+ ion, we have used the relation between $T_e(\text{O II})$ and $T_e(\text{O III})$ (ITL94), based on the photoionization models of Stasińska (1990). $T_e(\text{O II})$ has been used to derive the O^+ , N^+ and Fe^+ ionic abundances. For Ar^{2+} and S^{2+} we have used an electron temperature intermediate between $T_e(\text{O III})$ and $T_e(\text{O II})$ following the prescriptions of Garnett (1992).

Total element abundances have been derived after correction for unseen stages of ionization as described by ITL94. The spectrum of SBS 1415+437 shows a strong nebular He II $\lambda 4686$ emission line, implying the presence of a non-negligible amount of O^{3+} . Its abundance is derived from the relation:

$$\text{O}^{3+} = \frac{\text{He}^{2+}}{\text{He}^+} (\text{O}^+ + \text{O}^{2+}). \quad (3)$$

Then, the total oxygen abundance is equal to

$$\text{O} = \text{O}^+ + \text{O}^{2+} + \text{O}^{3+}. \quad (4)$$

The electron temperatures, number densities, ionic and total element abundances along with ionization correction factors are shown in Table 3.

To derive carbon and silicon abundances we adopt the electron temperature obtained from the MMT small aperture spectrum as the latter has a much better signal-to-noise ratio than the FOS spectrum. This is legitimate as the area of the small square aperture of the MMT spectrum is only 1.55 times that of the FOS aperture, similar to the ratio 1.47 of the $\text{H}\beta$ fluxes in the two apertures.

We derive the C^{2+} abundance from the relation (Aller 1984, p.125-126):

$$\frac{\text{C}^{2+}}{\text{O}^{2+}} = 0.093 \exp\left(\frac{4.656}{t}\right) \frac{I(\text{CIII})\lambda 1906 + \lambda 1909}{I([\text{OIII}]\lambda 4959 + \lambda 5007)}, \quad (5)$$

where $t = T_e/10^4$. Following Garnett et al. (1995a) we adopt for the temperature in Eq. (5) the value $T_e(\text{O III}) = 16600 \pm 270$ K derived from the spectrum in the small MMT aperture. As the $\text{O III}] \lambda 1666$ emission line is not seen, we cannot derive an extinction-independent $\text{C}^{2+}/\text{O}^{2+}$ ratio. However, the extinction derived from the FOS spectrum is very small ($C(H\beta) = 0.02$ dex). Assuming $C(H\beta) = 0$ we derive $\text{C}^{2+}/\text{O}^{2+}$, about 5 % lower than the value in Table 3. Adopting $T_e(\text{O III}) = 17100 \pm 2700$ K as derived from the noisier FOS spectrum we obtain a very similar $\text{C}^{2+}/\text{O}^{2+}$ ratio. We calculate the correction factor $\text{ICF}(\text{C})$ for unseen ionization stages of carbon following Garnett et al. (1995a). In the case of SBS 1415+437 the correction is small, $\text{ICF}(\text{C})$ being equal to 1.05.

The silicon abundance is derived following Garnett et al. (1995b) from the relation

$$\frac{\text{Si}}{\text{C}} = \text{ICF}(\text{Si}) \frac{\text{Si}^{2+}}{\text{C}^{2+}}, \quad (6)$$

where

$$\frac{\text{Si}^{2+}}{\text{C}^{2+}} = 0.188t^{0.2} \exp\left(\frac{0.08}{t}\right) \frac{I(\text{SiIII})\lambda 1883 + \lambda 1892}{I(\text{CIII})\lambda 1906 + \lambda 1909)}. \quad (7)$$

For the determination of the silicon abundance we again adopt the temperature $T_e(\text{O III}) = 16600 \pm 270$ K. The correction factor $\text{ICF}(\text{Si}) = 1.33$ is derived following Garnett et al. (1995b). As discussed before,

we have assumed $I(\text{Si III}] \lambda 1883 + \lambda 1892) = 1.67 \times I(\text{Si III}] \lambda 1883)$ since the $\text{Si III}] \lambda 1892$ emission line is not seen, although the signal-to-noise ratio of the spectrum and the intensity of the $\text{Si III}] \lambda 1883$ emission line imply that it should be present.

3.2. Heavy element abundances and age constraints

The heavy element abundances in SBS 1415+437 corresponding to the two MMT apertures and those corresponding to the *HST* FOS aperture are shown in Table 3. They are in very good general agreement with the values derived by Izotov & Thuan (1998b, 1999) from 4-meter Kitt Peak telescope observations. In particular, the oxygen abundance derived by Izotov & Thuan (1999) is $12 + \log(\text{O}/\text{H}) = 7.59 \pm 0.01$. The ratios of α -process elements Ne, S, Ar abundances to O abundance are in very good agreement with the mean values derived for low-metallicity blue compact galaxies by Thuan, Izotov & Lipovetsky (1995, hereafter TIL95) and Izotov & Thuan (1999).

We find that the N/O ratios derived from both MMT spectra ($\log(\text{N}/\text{O}) = -1.54 \pm 0.03$ and -1.55 ± 0.03) are in agreement with the mean value $\log(\text{N}/\text{O}) = -1.53 \pm 0.08$ derived by TIL95 for their sample of very metal-deficient BCDs, but are slightly higher than the value -1.58 ± 0.02 derived by Izotov & Thuan (1998b) for this galaxy from 4-meter Kitt Peak telescope observations. The small difference may be due to a larger contamination in the lower spectral resolution MMT spectrum of the $[\text{N II}] \lambda 6584$ emission line by the strong nearby $\text{H}\alpha \lambda 6563$ emission line. In spite of these small subtle differences, all determinations of the N/O ratio in SBS 1415+437 are in agreement within the errors. Hence, SBS 1415+437 falls within the narrow range of N/O ratios found in other low-metallicity BCDs. For BCDs with $12 + \log(\text{O}/\text{H}) \lesssim 7.6$, TIL95 and Izotov & Thuan (1999) found that the dispersion about the mean of the N/O ratio is remarkably small, being only 0.02 dex. The constancy of N/O with O abundance implies that N and O share the same origin. Moreover, the very small dispersion is strong evidence against time-delayed production of primary N and supports the view that primary N in galaxies with $Z \lesssim Z_{\odot}/20$ is produced by massive ($M > 9 M_{\odot}$) stars only. Intermediate-mass ($3 M_{\odot} \lesssim M \lesssim 9 M_{\odot}$) stars in those galaxies have not had time enough to evolve to contribute primary N. Hence, the observed N/O ratio in SBS 1415+437 implies that it is a young galaxy with an age not exceeding ~ 100

Myr (the lifetime of a $9 M_{\odot}$ star being ~ 40 Myr).

Another important age discriminator is the Fe/O ratio. While oxygen is produced only by massive stars, production of iron occurs not only during explosive nucleosynthesis in massive stars, but also in SNe I about 1 Gyr after the beginning of star formation in the BCD. In the latter case a nearly solar Fe/O ratio is expected. However, TIL95 and Izotov & Thuan (1999) have shown that at low metallicities ($12 + \log(\text{O}/\text{H}) \lesssim 8.2$), O is overproduced with respect to Fe as compared to the solar neighborhood. The mean value $[\text{O}/\text{Fe}] (= \log(\text{O}/\text{Fe}) - \log(\text{O}/\text{Fe})_{\odot})$ for low-metallicity BCDs is 0.32 ± 0.11 (Izotov & Thuan 1999) and compares well with values observed in Milky Way halo stars (TIL95). In SBS 1415+437, we find $[\text{O}/\text{Fe}] = 0.27 \pm 0.03$ and 0.30 ± 0.07 respectively for the large and small apertures. These values are consistent within the errors with the mean value for low-metallicity BCDs, although the value for the small aperture is more uncertain due to the weakness of $[\text{Fe III}] \lambda 4658$ emission line and its possible contamination by the Wolf-Rayet C IV $\lambda 4658$ line. The second possibility is less likely however, as no other broad Wolf-Rayet lines are seen in the small aperture spectrum. The high $[\text{O}/\text{Fe}]$ value seen in SBS 1415+437 as compared to the solar neighborhood also suggests a small age for this galaxy, although it can be explained, in principle, by depletion of iron into dust grains.

Further chemical constraints on the age of SBS 1415+437 come from *HST* FOS spectroscopy. We show the C/O abundance ratio vs. oxygen abundance in Figure 3a and the Si/O abundance ratio vs. oxygen abundance in Figure 3b. The filled circle represents SBS 1415+437 while open circles represent data from Izotov & Thuan (1999). The silicon-to-oxygen abundance ratio in SBS 1415+437 ($\log(\text{Si}/\text{O}) = -1.46 \pm 0.27$) agrees well with the solar value ($\log(\text{Si}/\text{O})_{\odot} = -1.38$). It is independent of O abundance as expected since both Si and O have the same origin: they are both produced by high-mass stars. Although errors in the determinations of the Si abundances are still large, there is no evidence for significant depletion of silicon into dust grains as suggested by Garnett et al. (1995b). This would argue for no depletion of iron in SBS 1415+437 as well.

While silicon is produced only by high-mass stars, carbon is a primary element produced by both intermediate and high-mass stars. Therefore, the C/O ratio is a sensitive indicator of the age of a galaxy

(Izotov & Thuan 1999). Figure 3a shows that the value of $\log(C/O) = -0.78 \pm 0.10$ in SBS 1415+437 is in good agreement with those derived for other low-metallicity BCDs with $12 + \log(O/H) \lesssim 7.6$ (Izotov & Thuan 1999). The observed $\log(C/O)$ in SBS 1415+437 is consistent with the value of ~ -0.83 predicted by the theory of massive star nucleosynthesis (Weaver & Woosley 1993; Woosley & Weaver 1995) and with $\log(C/O)$ observed in halo stars (Tomkin et al. 1992). This suggests that the carbon seen in the BCD has been made by high-mass stars only, and that intermediate-mass stars have not had enough time to evolve and add their own C contribution. As in the case of N/O, the value of the C/O ratio allows us to say that the first star formation in SBS 1415+437 has not occurred more than ~ 100 Myr ago.

In summary, the analysis of the relative heavy element abundance ratios in SBS 1415+437 has led us to an important conclusion: all observed species have been made by massive stars. The absence of evidence of any element production by intermediate-mass stars allows to put an age upper limit of ~ 100 Myr for the BCD.

3.3. Spatial distribution of heavy element abundances

The spatial distribution of element abundances provides important constraints on the enrichment and mixing processes in the interstellar medium of galaxies. Kobulnicky & Skillman (1996) discussed this problem for the metal-rich dwarf galaxy NGC 4214, and show that inside H II regions the material is well mixed and is characterized by nearly constant element abundances. In low-metallicity environments, such studies have been carried out by Martin (1996) for I Zw 18 and by Izotov et al. (1997a) for SBS 0335-052. The results were very similar. Martin (1996) found the oxygen abundance to be nearly constant inside the central 530 pc of I Zw 18 and to be within 20 % of the abundance in the NW H II region ($12 + \log(O/H) = 7.1 - 7.3$). She argued that the detection of a superbubble in I Zw 18 implies a timescale of $\sim 15 - 27$ Myr and a spatial scale of ~ 900 pc for dispersing the recently synthesized elements. Izotov et al. (1997a) found the constancy of the heavy element abundances to hold within the errors at even larger scales in SBS 0335-052, over the central 2 kpc around the youngest cluster.

Large abundance variations have been seen in only two galaxies thus far. Walsh & Roy (1987, 1989)

found the N/O ratio in different knots in the starburst galaxy NGC 5253 to vary by factors of up to 3 and that these variations are associated with the presence of Wolf-Rayet stars of WN type. A more extreme case is that of the BCD Mkn 996 (Thuan, Izotov & Lipovetsky 1996) where the N/O ratio in the extremely compact central part of the galaxy is a factor of ~ 25 greater than the mean value found in BCDs, and decreases steeply outward. Local nitrogen enrichment in Mkn 996 is associated with WN stars as well. Both these galaxies are however relatively more metal-rich ($Z \gtrsim Z_{\odot}/10$) and the nuclear H II region in Mkn 996 is some five orders of magnitude denser (its N_e is $\sim 10^7 \text{ cm}^{-3}$) than typical H II regions in BCDs.

SBS 1415+437 is on the other hand a more typical low-metallicity BCD. Figure 4 shows the spatial variations of the electron temperature, oxygen abundance, and abundance ratios of various heavy elements relative to oxygen along the major axis of the galaxy. Data for two distinct H II regions are presented, that for the brightest H II region at the SW edge of the SBS 1415+437 and that for the H II region at $16''$ (~ 880 pc) in the NE direction from it. Although [O III] $\lambda 5007$ and H α emission are observed everywhere between these two H II regions, the emission lines are too weak for abundance measurements. The abundances are derived from one-dimensional spectra extracted from the MMT two-dimensional spectrum. The auroral [O III] $\lambda 4363$ emission line is detected only in the brightest region, $\sim 5''$ along the slit, allowing a direct determination of $T_e(\text{O III})$. In the spectra where the [O III] $\lambda 4363$ emission line is not seen, we use the approximation

$$t_e(\text{OIII}) = 2.63 - 1.37 \times \log \left[\frac{I(\lambda 3727 + \lambda 4959 + \lambda 5007)}{I(\text{H}\beta)} \right], \quad (8)$$

where $t_e = T_e/10^4$. The above equation was derived using the sample of low-metallicity BCDs of ITL94, ITL97 and TIL95 with $12 + \log(O/H) \lesssim 7.9$ and precise electron temperature determinations (the mean error in T_e is ~ 1000 K).

Inspection of Figure 4 shows that the electron temperature and element abundances within the brightest H II region are remarkably constant with radius, out to ~ 350 pc. The fainter H II region appears to show a slight decrease in oxygen abundance at the furthest point, when $12 + \log(O/H)$ drops below 7.4, although the difference is not significant. We conclude that in SBS 1415+437 just as in SBS 0335-052, the elemental

abundances do not vary within the errors, although the spatial scales probed are smaller. In subsection 3.2, we have concluded that the H II regions in SBS 1415+437 are most likely enriched by the products of nucleosynthesis in massive stars. Since the lifetime of massive stars is in the range $10^6 - 10^7$ yr, the time scale for the enrichment of the ionized gas with heavy elements is also of the same order. The constancy of the heavy element abundances is consistent with a scenario of self-enrichment of the gas followed by rapid mixing. A scenario of self-enrichment of giant H II regions has been proposed by Kunth & Sargent (1986), who suggested that new heavy element ejecta from supernovae of type II and stellar winds initially mix exclusively with the ionized gas in the H II zone, while further mixing with the cold gas happens only later during the long interburst phase. Roy & Kunth (1995) have analyzed different mechanisms of interstellar medium mixing and found that the ionized gas is well mixed due to Rayleigh-Taylor and Kelvin-Helmholtz instabilities on time scales of $\sim 1.5 \times 10^6$ yr within regions of ~ 100 pc size. The enriched gas in the H II regions can be easily transported by expanding shells of supernovae and stellar winds in a short time scale. Such a picture is also supported by the observation of ionized gas velocities of order 10^3 km s $^{-1}$ in several dwarf galaxies (Roy et al. 1992, Skillman & Kennicutt 1993 and Izotov et al. 1996). The presence of several superbubbles in the WFPC2 images of SBS 1415+437 suggest that these fast motions are likely to be also present in the BCD.

3.4. Helium Abundance

The extremely low oxygen abundance of SBS 1415 + 437 ($Z_{\odot}/21$) as well as the high surface brightness of its star-forming region implies that the galaxy is one of the best objects for primordial helium abundance determination. The high S/N ratio spectrum obtained for SBS 1415+437 (Figure 1) allows us to measure helium line intensities with good accuracy. The He I line intensities corrected for interstellar extinction are shown in Table 2 for both the large and small apertures. For helium abundance determination we use the He I $\lambda 4471$, $\lambda 5876$ and $\lambda 6678$ emission lines. However, the He I line intensities deviate from their pure recombination values and must be corrected for several mechanisms (ITL97, Izotov & Thuan 1998ab). One of the main mechanism is collisional excitation from the metastable 2^3S level. This

mechanism depends on the electron temperature and electron number density. The line most sensitive to collisional enhancement in the optical range is He I $\lambda 7065$. Another mechanism is self-absorption in some optically thick emission lines, such as He I $\lambda 3889$. The emission lines most sensitive to this fluorescence mechanism are He I $\lambda 3889$ and $\lambda 7065$. In contrast to collisional enhancement, which increases the intensities of all He I lines, the fluorescence mechanism works in such a way as to decrease the intensity of the He I $\lambda 3889$ line as its optical depth increases, while increasing the intensities of other lines of interest (He I $\lambda 4471$, $\lambda 5876$, $\lambda 6678$ and $\lambda 7065$). And, finally, underlying He I stellar absorption lines produced by O and B stars which decrease the He I emission line intensities, has to be taken into account. To correct the He I emission line intensities for collisional and fluorescent enhancement we follow the approach described by ITL97 and Izotov & Thuan (1998b). We assume that the electron temperature in the He $^+$ zone is equal to that in the O $^{2+}$ zone. However, we do not set its electron number density equal to that derived from the [S II] $\lambda 6717/\lambda 6731$ line ratio for two reasons: (1) the S $^+$ and He $^+$ zones do not coincide; (2) although an electron number density $N_e(\text{S II}) = 80$ cm $^{-3}$ was derived in the large aperture, a much smaller value is obtained in the small aperture. We adopt the value of 10 cm $^{-3}$. Both $N_e(\text{S II})$ values are small and subject to large uncertainties because the sulfur emission line intensity ratio [S II] $\lambda 6717/\lambda 6731$ is not sensitive to N_e at these low number densities. Therefore we use the intensities of the 5 He I $\lambda 3889$, $\lambda 4471$, $\lambda 5876$, $\lambda 6678$ and $\lambda 7065$ emission lines to solve self-consistently for 1) the electron number density in the He $^+$ zone $N_e(\text{He}^+)$ and 2) the optical depth $\tau(\lambda 3889)$ in the He I $\lambda 3889$ line, to reproduce the theoretical He I line intensity recombination ratios.

The best solution for both apertures gives $N_e(\text{He}^+) = 10$ cm $^{-3}$ and $\tau(\lambda 3889) = 0.1$. The helium abundance for individual lines along with their correction factors for collisional and fluorescent enhancement are given in Table 4. The helium mass fraction in SBS 1415+437, $Y = 0.246 \pm 0.004$ for the large aperture and $Y = 0.245 \pm 0.005$ for the small aperture, compares well with the value 0.244 ± 0.002 derived by Izotov & Thuan (1998b) for this galaxy. It is in good agreement with that derived for other low-metallicity BCDs and is close to the primordial helium mass fraction $Y_p = 0.244 \pm 0.002$ derived by Izotov & Thuan (1998b). Note that in general, the corrections to the

He I line intensities are small because the H II region in SBS 1415+437 is not so hot and dense as that in the more metal-deficient BCD SBS 0335–052 (Izotov et al. 1997a). The $H\beta$ equivalent widths of 159 Å for the large aperture and 140 Å for the small aperture, are large compared to the value of 56 Å measured in the NW component of I Zw 18 (Izotov et al. 1997b). Therefore, the equivalent widths of the He I emission lines are larger as well and underlying stellar absorption does not play as important a role as in the case of I Zw 18.

4. MORPHOLOGY AND KINEMATICS OF THE IONIZED GAS

We display in Figure 5 the I image of SBS 1415+437 with the contrast level adjusted so as to show the low-surface-brightness underlying extended component. The galaxy has an elongated shape with a bright H II region at its SW tip and belongs to the class of “cometary galaxies” in the BCD classification scheme of Loose & Thuan (1985). Many point sources are seen which are identified as luminous stars. To the SW of brightest H II region, two stellar clusters with resolved stars are present. Although we have not observed these two clusters spectroscopically, they are likely at the same distance as the main body of the galaxy, since they are connected to it by diffuse low-surface-brightness light. The rest of the light comes from an unresolved lower surface brightness extended stellar component. The magnified I image of the bright H II region (Figure 6) shows resolved luminous stars which are nearly aligned, implying propagating star formation. The structure of the star-forming region in SBS 1415+437 is different from that observed in SBS 0335–052 where several luminous compact super-star clusters are seen (Thuan, Izotov & Lipovetsky 1997). Instead, star-formation in SBS 1415+437 is more quiescent and is more similar to what is observed in I Zw 18 (Hunter & Thronson 1995). It appears that the mode of star formation varies in different BCDs. The BCD’s total mass may play a role: SBS 0335–052 where star formation occurs in super-star clusters has a H I mass ~ 6 times greater than that in SBS 1415+437 (Thuan et al. 1999a).

In Figure 7 we show the $(V - I)$ color map of SBS 1415+437, where dark denotes blue colors and light denotes red colors. The very blue H II regions in the SW tip can be seen, together with extended emission with a moderately blue color and red supergiant stars

(white points) along the main body of the galaxy. The southernmost of the two H II regions seen to the SW of the brightest H II region is very blue, while in the other H II region red supergiants are already present. The structure of the brightest H II region in the $(V - I)$ image is very filamentary, as seen better in the magnified picture (Figure 8). This filamentary structure is caused in part by the presence of super-shells of ionized gas delineating supernova cavities, and in part by the presence of dust patches, as evidenced by the extinction coefficient $C(H\beta) = 0.12$ dex derived from the spectrum in the large aperture. Figure 9 shows that there is a systematic reddening of the $(V - I)$ color for the stars in the chain seen in Figure 6, away from the star at the southernmost tip, implying propagating star formation from the NE to the SW.

A long-exposure long-slit MMT spectrum shows that [O III] $\lambda 5007$ and $H\alpha$ emission are present along most of the body of SBS 1415+437 which has an angular diameter of 46'' at the surface brightness isophote of 25 mag arcsec⁻². Only the outermost 13'' of the galaxy at the NE side do not show emission lines. We measure the wavelength shifts of these two lines to derive radial velocities and a rotation curve. The velocity distribution along the major axis of SBS 1415+437 is shown in Figure 10. As the velocities derived from each of the lines do not show significant systematic relative shifts, we have fitted a linear relation to the data, between the radial velocity and the location along the slit, using a maximum likelihood method. The origin in distance is taken to be at the maximum of the brightness distribution. The resulting linear regression is shown by the solid line. The velocity profile clearly indicates solid-body rotation in SBS 1415+437, with a rotational velocity of ~ 50 km s⁻¹ over the part of the galaxy with emission lines, i.e. a region with a spatial angular extent of $\sim 30''$. Extrapolation of the rotation curve to the whole diameter of 46'' gives a rotational velocity $v_{rot} = 80$ km s⁻¹. This yields a dynamical mass $M_T = G^{-1} r v_{rot}^2 \sim 1.9 \times 10^9 M_\odot$. Since the H I mass is $1.48 \times 10^8 M_\odot$ (Thuan et al. 1999a), this gives a $M(\text{H I})/M_T$ ratio of 0.08, in the range of the values obtained in other BCDs such as I Zw 36 (0.14, Viallefond & Thuan 1983) or I Zw 18 (0.10, van Zee et al. 1998). As the mass of the visible stellar population does not exceed $\sim 10^6 M_\odot$ (see section below), a large part of the mass of SBS 1415+437 is dark.

5. STELLAR POPULATIONS

5.1. Surface brightness and color distributions

Surface photometry was done by fitting ellipses to isophotal contours using the task ELLIPSE in STSDAS. We show in Figure 11a the V and I surface brightness distributions as a function of r , the equivalent radius of the best fitting elliptical isophote defined as $r = \sqrt{ab}$, where a and b are respectively the semi-major and semi-minor axes of the ellipse. Both V and I surface brightness profiles (SBP) can be fitted for $r \geq 4''$ by an exponential law of the form $I = I_0 \exp(-\alpha)$, characteristic of a disk structure. The best fits to the outer parts are shown by straight lines in Figure 11a and are given by:

$$\mu_V = (21.00 \pm 0.04) + (0.205 \pm 0.005)r, \quad (9)$$

$$\mu_I = (20.69 \pm 0.03) + (0.197 \pm 0.004)r. \quad (10)$$

This corresponds to scale-lengths $\alpha_V^{-1} = \alpha_I^{-1} = 0.27$ kpc, in the lower range of the values found for BCDs (Papaderos et al. 1996, Lipovetsky et al. 1999b). The central surface brightnesses are $\mu_{V_0} = 21.00$ mag arcsec $^{-2}$ and $\mu_{I_0} = 20.69$ mag arcsec $^{-2}$ as Galactic extinction is negligible (Burstein & Heiles 1982). The rise above the exponential law for $r \leq 3''$ is caused by the bright star-forming region.

Figure 11b shows the $(V - I)$ color profile of SBS 1415+437. The very blue color at the center ($(V - I) \lesssim 0.0$ for $r \lesssim 2''$) is due to the bright star-forming region. The galaxy becomes gradually redder with increasing r reaching a constant $(V - I) \sim 0.4$ at $r \geq 5''$. This constant color is that of the underlying low-surface-brightness component. The V_{25} isophotal radius at the surface brightness level of 25 mag arcsec $^{-2}$ is $16''$, corresponding to a linear radius of 0.88 kpc. Total magnitudes inside the 25 mag arcsec $^{-2}$ isophotal level are $V = 15.55 \pm 0.01$ mag and $I = 15.47 \pm 0.01$ mag. Adopting $B = 15.60$ mag (Lipovetsky et al. 1999b), we derive $L_B = 1.2 \times 10^8 L_{B\odot}$, giving $(M_{\text{HI}}/L_B)/(M/L_B)_{\odot} = 1.3$ and $(M_T/L_B)/(M/L_B)_{\odot} = 16$. These ratios are relatively high compared the respective mean values of 0.6 and 5 obtained by Thuan (1985) for a large sample of BCDs. This indicates that a relatively small fraction of the gas in SBS 1415+437 has been converted into stars and supports the conclusion that the BCD is young.

The blue $(V - I)$ color (~ 0.4 mag) of the extended underlying low-surface-brightness stellar component

is remarkable. This color is as blue as the $(V - I)$ color corrected for gaseous emission of the underlying component of SBS 0335-052 which Thuan et al. (1997) and Izotov et al. (1997a) have argued to be a young galaxy, with stars not older than ~ 100 Myr. Comparison with evolutionary synthesis models (Leitherer & Heckman 1995; Tantalo et al. 1996) also gives an upper limit for the age of the stellar populations in SBS 1415+437 of ~ 100 Myr. These models predict a $(M/L_B)/(M/L_B)_{\odot}$ ratio of ~ 0.01 for an age of 100 Myr, giving a stellar mass of $1.2 \times 10^6 M_{\odot}$. Direct age determinations for the stellar populations in SBS 1415+437 can be obtained from color-magnitude diagrams which we discuss next.

5.2. Color-magnitude diagrams

The superior spatial resolution of *HST* WFPC2 images combined with the proximity of SBS 1415+437 permits to resolve individual stars and study stellar populations in this galaxy by means of color-magnitude diagrams (CMD). We used the DAOPHOT routine PSF to fit the point spread function and measure the brightness of individual stars. Figure 12 shows the distribution of photometric errors as a function of V and I magnitudes as determined by DAOPHOT. We see that errors are of order 0.3 mag at 27 mag in V and I , increasing to ~ 0.5 mag at 28 mag.

We have carried out a completeness analysis using the DAOPHOT routine ADDSTAR. For each frame we have added artificial stars amounting to ~ 10 % of the real stars detected in each magnitude bin in the original image. We then performed a new photometric reduction using the same procedure as the one applied to the original frame, and checked how many added stars were recovered. This operation was repeated 10 - 20 times for each frame and the results were averaged. The completeness factor in each magnitude bin defined as the percentage of recovered artificial stars is shown in Table 5. It can be seen that the completeness limit is reasonably good, 83 % and 70 % respectively at V , $I \sim 25$ mag, but drops to 22 % and 4 % at 27 mag. The total numbers of recovered stars in the frame are respectively 3677, 5652 and 1020 in the F569W band, the F791W band and in both of these bands at the same time.

We decided not to construct a CMD for the entire galaxy as is usually done (e.g. Dohm-Palmer et al. 1997ab, Schulte-Ladbeck, Crone & Hopp 1998). Rather, because the morphology of SBS 1415+437

and spectroscopic observations suggest propagating star formation from the NE to the SW, we have divided the BCD into 6 regions labeled from I to VI as shown in Figure 13, and constructed separate CMDs for each of these regions. The total number of stars in the 6 CMDs is 785. The F569W and F791W magnitudes are measured within a 2-pixel radius circular aperture, and then converted to magnitudes within a 0.5 arcsec radius circular aperture using the correction factors of Holtzman et al. (1995a).

The correction for internal extinction poses a problem. The BCD is undergoing an intense burst of star formation, and dust is expected to be produced in expanding envelopes of supernovae. We have already noted that the $(V-I)$ color distribution in the brightest part of the BCD is inhomogeneous (Figure 7) implying the presence of dust patches. Dust is known to be present even in the most metal-deficient BCDs. A striking example is that of the BCD SBS 0335–052 with a metallicity of only 1/41 solar. It shows strong mid-infrared emission, implying a silicate dust mass of $\sim 10^4 M_{\odot}$ (Thuan, Sauvage & Madden 1999b). Dust patches mixed in the star-forming region can be clearly seen on *HST* pictures of SBS 0335–052 (Thuan et al. 1997), and spectroscopic observations (Izotov et al. 1997a) show the extinction to be high and to vary spatially. Spatial variations of the extinction can also be seen in SBS 1415+437. Spectral observations of the brightest H II region (region III) in different apertures show $E(B-V)$ varying from 0.01 to 0.08 mag (Table 2), on a scale less than 240 pc. The extinction is even larger ($E(B-V) = 0.18$ mag or $A_V = 0.6$ mag) in other parts of the BCD (subsection 5.3). These spatial variations of the extinction introduce uncertainties in the derived CMDs. As a first approximation, we correct the CMD for each region by a constant internal extinction, when the spectral data are good enough to allow extinction estimates from the observed Balmer decrements (see subsection 5.3). The CMD for region III has been corrected for extinction corresponding to $A_V = 0.25$ mag and $A_I = 0.15$ mag, while the CMDs for regions IV – VI have been corrected for extinction corresponding to $A_V = 0.55$ mag and $A_I = 0.41$ mag. The CMDs for regions I and II have not been corrected for internal extinction for lack of information. In those CMDs, stars are fainter and redder than they really should be. Therefore, the comparison of the location of stars with isochrones in those CMDs gives only upper limits on their ages.

The $(V-I)$ vs. I diagrams for each region are shown in Figure 14 together with stellar isochrones by Bertelli et al. (1994) for a heavy element abundance of 1/20 the solar value. Each isochrone is labeled by the logarithm of the age in yr. In Figures 14 c-f, the region occupied by 1 Gyr or older asymptotic giant branch (AGB) stars is shown by dashed lines while the observational limits are shown by a dotted line. For the latter, we adopt the magnitude limits $V = I = 28$ mag as suggested by Figure 12. None of the stars lie beyond this line as they should.

We now discuss the ages (or their upper limits) of the stellar populations in each region. The small regions I and II lie outside the main body of the BCD to the SW of the brightest H II region, and contain two young stellar clusters. Inspection of the $(V-I)$ color maps in Figures 7 and 8 shows that they have different ages. While red supergiants are present in region II, they are absent in region I which is dominated by ionized gas indicative of the presence of hot O stars. The CMDs confirm that scenario: all stars in region I (Figure 14a) are still on the main sequence. Region II is more evolved and has an age $\gtrsim 10$ Myr (Figure 14b). Region III contains the brightest H II region (Figure 12). Its CMD (Figure 14c) shows a mixture of stellar populations with different ages, ranging from $\lesssim 10$ Myr to 100 Myr. There appears to be red stars present in region III, with absolute magnitude M_I in the range -5.5 to -6.5 mag and $(V-I)$ color in the range 1.0 to 2.0 mag. However the colors of these red stars are quite uncertain: they have $I \sim 25.5$ mag, or $V \sim 27.5$ mag, so that their $(V-I)$ colors can have errors as large as 0.4 mag. If real, these red stars can be either young AGB stars with age ~ 100 Myr or red supergiant (RSG) stars (Gallart et al. 1996).

Because of the distance of SBS 1415+437, the imaging data presented here is not capable of detecting a 1 Gyr or older AGB stellar population, even if it exists. At $V, I = 26$ mag, where the completeness is respectively 59 % and 35 % (Table 5), the detection limit for $(V-I) = 2$ mag is $I = 24$ mag, nearly 1 mag above the AGB (upper dashed horizontal line in Fig. 14). By going down to $V, I = 27$ mag which would allow to reach the AGB, the completeness limits drop precipitously to 22 % and 4 %. Thus our CMDs cannot be used to exclude the presence of an old AGB stellar population. They can only provide a useful consistency check for stellar population ages derived by other techniques. Thus, the young ages inferred for the detected stars in region III from its CMD are

in good agreement with those derived from the blue integrated ($V - I$) color of -0.07 mag obtained by surface photometry (Table 5) and with those obtained from modeling the spectral energy distributions (subsection 5.3).

The stellar populations in regions IV to VI are similar to those in region III except that the very youngest population with age less 10 Myr is not present (Figures 14 d-f). Evolutionary synthesis models considered in subsection 5.3 give also an age $\lesssim 100$ Myr for regions IV to VI. From the CMD analysis, there is clear evidence for propagating star formation in SBS 1415+437 from the NE (region VI) to the SW (region I). The CMDs show an evident trend of increasing age from region I to region VI. On smaller spatial scales, the same propagating star formation is seen within region III where the brightest stars are distributed along a line in the NE - SW direction (Figure 6), with increasing age from the SW to NE (Figure 9).

5.3. Evolutionary synthesis models and the age of SBS 1415+437

Stronger evidence in favor of the evolutionary youth of SBS 1415+437 is provided by the spectral energy distributions (SED) of regions III through VI as shown in Figure 15. All spectra are very blue. The spectrum of region III (Figure 15a) contains many nebular emission lines: evidently, the continuum is dominated by the light of a very young O star population. The spectra of the other regions (Figures 14 b-d) indicate older populations: their slopes are less steep and they show strong hydrogen Balmer absorption lines characteristic of B and A stars.

To estimate quantitatively the age of each region, we calculate a grid of SEDs for stellar populations with ages varying between 10 Myr and 20 Gyr and with a heavy element abundance $Z_{\odot}/20$, following the method described in Papaderos et al. (1998). Briefly, we use isochrones of stellar parameters from Bertelli et al. (1994) and the compilation of stellar atmosphere models from Lejeune, Cuisinier & Buser (1998). A Salpeter Initial Mass Function (IMF) with slope -2.35 , an upper mass limit of $100 M_{\odot}$ and a lower mass limit of $0.6 M_{\odot}$ were adopted. For stellar populations with age less than 10 Myr, we use the theoretical SEDs of Schaerer & Vacca (1998) corresponding to a heavy element mass fraction $Z_{\odot}/20$ and a Salpeter IMF. The stellar emission in SBS 1415+437 is contaminated by ionized gas emission from super-

giant H II regions. Therefore, to study the stellar populations in SBS 1415+437 it is necessary to construct a synthetic SED which includes both stellar and ionized gaseous emission. We have chosen not to calculate the contribution of ionized gas emission from the model value for the Lyman continuum luminosity. Instead, we add the gaseous spectral energy distribution derived from the observed line fluxes and equivalent widths, along with the observed emission lines in the spectral range $\lambda 3700 - 7500 \text{ \AA}$, to the calculated stellar spectral energy distribution. The gaseous emission contribution is scaled to the stellar emission by the ratio of the observed $H\beta$ equivalent width to the one expected for pure gaseous emission. The contribution of bound-free, free-free, two-photon continuum emission has been taken into account for the spectral range from 0 to $5 \mu\text{m}$ (Aller 1984; Ferland 1980). The effect of gaseous emission is important in region III, but is minor in the other regions as indicated by their small $H\beta$ equivalent width. For example, $EW(H\beta)$ is only 18 \AA in region V. We therefore neglect gaseous emission in regions IV - VI.

In order to compare the observed SEDs with the model SEDs, we need to correct the former for extinction. In many BCDs, the internal extinction derived from Balmer decrements significantly exceeds the Galactic extinction. This is the case for SBS 1415+437 where both imaging and spectroscopic data show the presence of significant internal extinction in the brightest H II region.

In Figure 16a the observed spectrum of region III (thin line) is shown along with the gaseous + synthetic stellar continuum produced by an instantaneous burst with age 4.7 Myr (thick line). The observed spectrum has been corrected for extinction, corresponding to $C(H\beta) = 0.12$ dex or $E(B - V) = 0.08$ mag as derived from the Balmer decrement. The agreement between the observed and model SEDs is very good, except in the $\lambda 3600 - 3900$ region where the model falls below the observed spectrum. The discrepancy is caused by the overlapping of the hydrogen Balmer absorption lines in the model SED. The inclusion of the observed Balmer hydrogen emission lines reduces the difference as shown in Figure 16b, where the contributions of gaseous and stellar emission are shown separately. It is evident from Figure 16b that the contribution of ionized gas emission to the total SED is significant in star-forming regions. This contribution is dependent on the equivalent width of $H\beta$ and the observed fluxes of other emission lines rela-

tive to $H\beta$. We present in Table 5 the model colors of a single stellar population with age 4.7 Myr. The calculated and observed ($V - I$) colors agree very well. Thus the bulk of the stellar population in region III is very young (~ 5 Myr), although stars as old as 100 Myr are also present, as shown by the CMD of this region (Fig. 14c). However, the contribution of the older stars to the total light is negligible.

Extinction correction is more of a problem when hydrogen emission lines are not present in the spectrum. Regions IV, V and VI are characterized by nearly identical spectral energy distributions (Fig. 15). However, only in region V are hydrogen emission lines present with a good enough signal-to-noise ratio to allow for the correction of internal extinction. Therefore only in that region can we derive the age of the stellar population.

To illustrate the effect of extinction on the derived age, we consider in turn both the extinction-uncorrected and corrected cases. As the reddening for the stellar continuum can be different (and is usually smaller) than that derived from the Balmer lines in the ionized gas (e.g. Calzetti, Kinney & Storchi-Bergmann 1994), the real situation lies somewhere between these two limiting cases. However, the following arguments show that the truth is closer to the case with extinction derived from the Balmer lines than to the case with no extinction. Figure 17a shows the spectrum of region V uncorrected for extinction, along with model SEDs for three different ages $\log t$ (yr) = 7.5, 8.0 and 8.1. The large difference between the model SEDs at $\log t = 8.0$ and 8.1 is due to the appearance of the first AGB stars in the latter case. The best fit is obtained for the model with $\log t = 8.1$. We present in Table 6 the model colors calculated for a single stellar population with $\log t$ varying between 7.2 and 8.1. It can be seen that the calculated ($V - I$) color of 0.79 mag for the age $\log t = 8.1$ is inconsistent with the color of ~ 0.4 derived from the HST images (this is the color of the flat part of the ($V - I$) color profile in Fig. 11b) and uncorrected for interstellar extinction. This is not too surprising as the extinction derived for region V from the Balmer decrement is high: $C(H\beta) = 0.26$ dex, equivalent to $A_V = 0.55$ mag and $A_I = 0.41$ mag. Figure 17b shows the extinction-corrected spectrum of region V with four model SEDs corresponding to $\log t = 7.2, 7.5, 8.0$ and 8.1. The best agreement between observation and model is achieved for a SED with $\log t$ between 7.2 and 8.0. These ages give a range of model ($V - I$)

colors between 0.21 and 0.43, which does include the observed color of 0.25, corrected for the interstellar extinction. Interpolating between the two colors gives $\log t = 7.25$ (see also Table 6). The above analysis shows the importance of extinction correction for age determination. Had we not corrected for extinction we would have derived an age $\log t = 8.1$ instead of $\log t = 7.3$, i.e. we would have overestimated the age by some 60 Myr. Extinction correction in region V makes stars brighter by 0.6 mag in V and by 0.4 mag in I , and red stars lie in the young supergiant region rather in the AGB region (Fig. 14e).

We stress here that evolutionary synthesis is a very sensitive technique for determining ages of stellar populations. We have used it to obtain ages of 5 and ~ 20 Myr for regions III and V, respectively. As the SEDs for regions IV and VI are very similar to that of region V (Fig. 15), it is likely that their stellar populations have ages of $\sim 20 - 100$ Myr. Thus, the analysis of stellar populations in SBS 1415+437 using evolutionary synthesis models has also led us to the conclusion that the galaxy is young. Star formation in the BCD did not start until ~ 100 Myr ago. This finding supports the conclusion of Izotov & Thuan (1999) based on the analysis of chemical abundances in a large sample of BCDs that all galaxies with metallicities $\lesssim Z_\odot/20$ are young, with ages less than ~ 100 Myr.

6. SUMMARY AND CONCLUSIONS

We have analyzed the properties and examined the evolutionary status of the nearby extremely low-metallicity ($Z_\odot/21$) blue compact dwarf (BCD) galaxy SBS 1415+437. Analysis of a very high signal-to-noise ratio long-slit MMT spectrum and of new *HST* FOS spectroscopy and WFPC2 imaging of the BCD has led us to the conclusion that SBS 1415+437 is a nearby *young* dwarf galaxy experiencing now its first burst of star formation which did not start until ~ 100 Myr ago. In particular, we have obtained the following results:

1. The oxygen abundance in SBS 1415+437 derived in two different apertures is very similar: $12 + \log(O/H) = 7.60 \pm 0.01$ and 7.61 ± 0.01 , respectively, i.e. only 1/21 of that of the Sun (adopting $12 + \log(O/H)_\odot = 8.93$ from Anders & Grevesse 1989). This is in excellent agreement with the value $12 + \log(O/H) = 7.59 \pm 0.01$ derived earlier by Izotov & Thuan (1998b) and in fair agreement with the value

$12 + \log(\text{O}/\text{H}) = 7.54 \pm 0.14$ derived from the lower signal-to-noise ratio *HST* FOS spectrum.

2. The α -elements-to-oxygen abundance ratios Ne/O, S/O, Ar/O in SBS 1415+437 are in very good agreement with the mean ratios for the most metal-deficient blue compact galaxies derived by Izotov & Thuan (1999). For the largest aperture, we derive $\log(\text{Ne}/\text{O}) = -0.75 \pm 0.02$ as compared to the mean value -0.75 ± 0.03 , $\log(\text{S}/\text{O}) = -1.58 \pm 0.02$ as compared to the mean value -1.59 ± 0.04 , and $\log(\text{Ar}/\text{O}) = -2.30 \pm 0.03$ as compared to the mean value -2.22 ± 0.07 . All these ratios are close to the respective solar ratios implying a common origin of α -elements in massive stars.

3. The nitrogen-to-oxygen abundance ratio $\log(\text{N}/\text{O}) = -1.54 \pm 0.03$ is in good agreement with the mean value of $\log(\text{N}/\text{O}) = -1.60 \pm 0.02$ derived by Izotov & Thuan (1999) for the most metal-deficient BCDs. The very small spread of the N/O ratio in the most metal-deficient BCDs ($Z \lesssim Z_{\odot}/20$) suggests that nitrogen in these galaxies is a *primary* element made only by *massive* stars. Intermediate-mass stars in these very metal-deficient BCDs have not had yet time to evolve and release their nucleosynthesis products. This implies that these galaxies, including SBS 1415+437, are not older than ~ 100 Myr (Izotov & Thuan 1999).

4. The iron-to-oxygen abundance ratio $[\text{O}/\text{Fe}] = 0.27 \pm 0.03$ is in excellent agreement with the mean value of 0.32 ± 0.11 derived by Izotov & Thuan (1999) for the most metal-deficient BCDs, and is similar to the values found in Galactic halo stars. Iron is produced only during explosive nucleosynthesis either by short-lived massive stars, progenitors of supernovae of type II or by long-lived low-mass stars, progenitors of supernovae of type I. Oxygen is overproduced relative to iron in SBS 1415+437 as compared to the Sun, suggesting that iron is produced by short-lived massive stars. Since SNe I start to explode after ~ 1 Gyr after the beginning of star formation, the $[\text{O}/\text{Fe}]$ value allows us to put an upper limit of 1 Gyr on the age of SBS 1415+437.

5. Carbon and silicon abundances have been derived using FOS *HST* observations. We find $\log(\text{C}/\text{O}) = -0.78 \pm 0.10$, in excellent agreement with the mean value of -0.78 ± 0.03 found by Izotov & Thuan (1999) for the most metal-deficient BCDs and that of -0.83 expected in the case of carbon production by massive stars only (Weaver & Woosley 1993). As in the case of nitrogen, the C/O ratio implies that

SBS 1415+437 is young enough so that intermediate-mass stars have not had time to evolve and release their C production. Again, this gives an upper limit for the age of SBS 1415+437 of ~ 100 Myr. As for Si, we find $\log(\text{Si}/\text{O}) = -1.46 \pm 0.27$ close to the solar value of -1.38 , as expected in the case of Si production in massive stars. We do not find significant Si depletion onto dust grains, contrary to the conclusion of Garnett et al. (1995b).

6. The heavy element abundances are constant within the largest supergiant H II region (region III) with a diameter of ~ 500 pc, similar to the spatial distribution of heavy elements in other extremely metal-deficient galaxies such as I Zw 18 (Martin 1996) and SBS 0335-052 (Izotov et al. 1997a). To within the errors, there are also no heavy element abundance variations in different H II regions within SBS 1415+437. This constancy strongly argues for H II region self-enrichment (Kunth & Sargent 1986).

7. SBS 1415+437 is one of the best targets for the determination of the primordial helium mass fraction Y_p because of its very low metallicity, high surface brightness and low electron number density which minimizes the influence of collisional enhancement of He I emission line intensities. The helium mass fraction in SBS 1415+437 is $Y = 0.246 \pm 0.004$, in very good agreement with the primordial value $Y_p = 0.244 \pm 0.002$ derived by Izotov & Thuan (1998b).

8. *HST* WFPC2 *V* and *I* images of SBS 1415+437 show a comet-like structure with a very blue bright supergiant H II region at its SW tip, and extended diffuse emission along the elongated main body of the galaxy on which are superposed red supergiant stars. The *V* and *I* surface brightness profiles are well fitted by exponentials with a very small scale-length $\alpha_V^{-1} = \alpha_I^{-1} = 0.19$ kpc and a central surface brightness $\mu_{V_0} = 21.00$ mag arcsec $^{-2}$ and $\mu_{I_0} = 20.69$ mag arcsec $^{-2}$. The $(V - I)$ color of the brightest H II region is very blue $\lesssim 0$. The galaxy becomes gradually redder with increasing distance from the brightest H II region, reaching a constant $(V - I) \sim 0.4$ at $r \gtrsim 5''$. These color changes imply changes in stellar population ages and propagating star formation in the BCD from the NE to the SW. Comparison of the observed colors with those of evolutionary synthesis models gives an upper limit for the age of the stellar populations of ~ 100 Myr. The resolved bright stars in the brightest H II region are also aligned along the NE - SW direction, supporting the hypothesis of the sequential character of star formation in SBS 1415+437. The $(V - I)$ color

image shows a filamentary structure caused by the superposition of many supernova supershells mixed in with dust patches. The H α and [O III] λ 5007 velocity distributions imply a solid-body rotation of the galaxy along the minor axis with a rotational velocity of 80 km s $^{-1}$. The dynamical mass within the optical diameter is $1.9 \times 10^9 M_{\odot}$ or ~ 13 times larger than neutral gas mass, indicating that the major part of the galaxy's mass is in the form of dark matter.

9. ($V - I$) - I color-magnitude diagrams (CMD) have been constructed for the stellar populations in 6 separate regions along the body of SBS 1415+437. We use MMT spectral observations to derive and correct for extinction for regions III to VI (Fig. 12), the spectra of regions I and II not showing strong enough Balmer lines to derive extinction. We have adopted as a first approximation a constant extinction in each region, although there is evidence that the extinction varies spatially on scales less than ~ 240 pc. The CMDs show a gradual increase of stellar population ages from the SW to NE, supporting the hypothesis of propagating star formation. SBS 1415+437 is too far away ($D = 11.4$ Mpc) for 1 Gyr or older asymptotic giant branch stars to be detected. Red stars are seen however with $(V - I) = 1 - 2$ mag, although these colors are subject to large errors (~ 0.4 mag). Corrected for extinction, their mean absolute magnitude M_I is ~ -5.5 to -6.5 mag, which makes them, if real, to be young red supergiant or young bright asymptotic giant branch stars with age $\lesssim 100$ Myr.

10. MMT long-slit spectroscopy along the major axis of SBS 1415+437 shows that everywhere in the galaxy, the spectral energy distribution (SED) is blue. We calculate model SEDs including both stellar and ionized gas emission for different regions in the galaxy, and found that the best fit for the brightest H II region gives a stellar age of ~ 5 Myr while the ages of the stellar populations in the other regions of the galaxy do not exceed 100 Myr.

In conclusion, chemical abundances, color profiles and evolutionary synthesis models for the spectral energy distribution all give an age of $\lesssim 100$ Myr for SBS 1415+437. The BCD is truly a young galaxy undergoing now its first burst of star formation. Along with I Zw 18 ($Z_{\odot}/50$, Hunter & Thronson 1995), SBS 0335-052 ($Z_{\odot}/41$, Thuan et al. 1997, Izotov et al. 1997a), SBS 1415+437 ($Z_{\odot}/21$) is the third extremely metal-deficient BCD, analyzed in detail for the age of its stellar populations, which confirms the conclusion of Izotov & Thuan (1999) that all galaxies with metal-

licities $\lesssim Z_{\odot}/20$ are young, with age not exceeding ~ 100 Myr.

Y.I.I. thanks the staff of the Astronomy Department of the University of Virginia for their kind hospitality. We thank Polis Papaderos for his help in deriving the surface brightness profiles. Partial financial support for this international collaboration was made possible by NATO collaborative research grant 921285 and NSF grant AST-9616863.

REFERENCES

- Aller, L. H. 1984, *Physics of Thermal Gaseous Nebulae* (Dordrecht: Reidel)
- Anders, E., & Grevesse, N. 1989, *Geochim. Cosmochim. Acta*, 53, 197
- Bertelli, G., Bressan, A., Chiosi, C., Fagotto, F., & Nasi, E. 1994, *A&AS*, 106, 275
- Brocklehurst, M. 1971, *MNRAS*, 153, 471
- Burstein, D., & Heiles, C. 1982, *AJ*, 87, 1165
- Calzetti, D., Kinney, A. L., & Storchi-Bergmann, T. 1994, *ApJ*, 429, 582
- Dohm-Palmer, R. C., Skillman, E. D., Saha, A., Tolstoy, E., Mateo, M., Gallagher, J., Hoessel, J., Chiosi, C., & Dufour, R. J. 1997a, *AJ*, 114, 2514
- . 1997b, *AJ*, 114, 2527
- Ferland, G. J. 1980, *PASP*, 92, 596
- Gallart, C., Aparicio, A., Bertelli, G., & Chiosi, C. 1996, *AJ*, 112, 2596
- Garnett, D. R. 1992, *AJ*, 103, 1330
- Garnett, D. R., Dufour, R. J., Peimbert, M., Torres-Peimbert, S., Shields, G. A., Skillman, E. D., Terlevich, E., & Terlevich, R. J. 1995b, *ApJ*, 449, L77
- Garnett, D. R., Skillman, E. D., Dufour, R. J., Peimbert, M., Torres-Peimbert, S., Terlevich, R., Terlevich, E., & Shields, G. 1995a, *ApJ*, 443, 64
- Garnett, D. R., Skillman, E. D., Dufour, R. J., & Shields, G. A. 1997, *ApJ*, 481, 174
- Holtzman, J. A., Burrows, C. J., Casertano, S., Hester, J. J., Trauger, J. T., Watson, A. M., & Worthey, G. 1995b, *PASP*, 107, 1065
- Holtzman, J. A., Hester, J. J., Casertano S., et al. 1995a, *PASP*, 107, 165
- Hunter, D. A., & Thronson, H. A. 1995, *ApJ*, 452, 238
- Izotov, Y. I., Dyak, A. B., Chaffee, F. H., Foltz, C. B., Kniazev, A. Y., & Lipovetsky, V. A. 1996, *ApJ*, 458, 524
- Izotov, Y. I., Foltz, C. B., Green, R. F., Guseva, N. G., & Thuan, T. X. 1997b, *ApJ*, 487, L37
- Izotov, Y. I., Lipovetsky, V. A., Chaffee, F. H., Foltz, C. B., Guseva, N. G., & Kniazev, A. Y. 1997a, *ApJ*, 476, 698
- Izotov, Y. I., Lipovetsky, V. A., Guseva, N. G., Kniazev, A. Y., & Stepanian, J. A. 1990, *Nature*, 343, 238
- Izotov, Y. I., & Thuan, T. X. 1998a, *ApJ*, 497, 227
- . 1998b, *ApJ*, 500, 188
- . 1999, *ApJ*, 511, 639
- Izotov, Y. I., Thuan, T. X., & Lipovetsky, V. A. 1994, *ApJ*, 435, 647 (ITL94)
- . 1997, *ApJS*, 108, 1 (ITL97)
- Kobulnicky, H. A., & Skillman, E. D. 1996, *ApJ*, 471, 211
- Kraan-Korteweg, R. C. 1986, *A&AS*, 66, 255
- Kunth, D., Maurogordato, S., & Vigroux, L. 1988, *A&A*, 204, 10
- Kunth, D., & Sargent, W. L. W. 1986, *ApJ*, 300, 496
- Landolt, A. U. 1992, *AJ*, 104, 340
- Leitherer, C., & Heckman, T. M. 1995, *ApJS*, 96, 9
- Lejeune, T., Cuisinier, F., & Buser, R. 1998, *A&AS*, 130, 65
- Lipovetsky, V. A., Chaffee, F. H., Izotov, Y. I., Foltz, C. B., Kniazev, A. Y., & Hopp, U. 1999a, *ApJ*, July 1
- Lipovetsky, V. A., Thuan, T. X., Kniazev, A. Y., Richter, G. M., Pustilnik, S. A., & Izotov, Y. I. 1999b, in preparation
- Loose, H.-H., & Thuan, T. X. 1985, in *Star-Forming Dwarf Galaxies*, ed. D. Kunth, T. X. Thuan and J. Tran Thanh Van (Gif-sur-Yvette: Editions Frontières), 73
- Martin, C. 1996, *ApJ*, 465, 680
- Oke, J.B. 1990, *AJ*, 99, 1621
- Papaderos, P., Izotov, Y. I., Fricke, K. J., Thuan, T. X., & Guseva, N. G. 1998, *A&A*, 338, 43
- Papaderos, P., Loose, H.-H., Thuan, T. X., & Fricke, K. J. 1996, *A&AS*, 120, 207
- Prévot, M. L., Lequeux, J., Maurice, E., Prévot, L., & Rocca-Volmerange, B. 1984, *A&A*, 132, 389
- Pustilnik, S. A., Thuan, T. X., Brinks, E., Lipovetsky, V. A., & Izotov, Y. I., 1999, in preparation
- Roy, J.-R., Aube, M., McCall, M. L., & Dufour, R. J. 1992, *ApJ*, 386, 498
- Roy, J.-R., & Kunth, D. 1995, *A&A*, 294, 432
- Schaerer, D., & Vacca, W. D. 1998, *ApJ*, 497, 618

- Schulte-Ladbeck, R. E., Crone, M. M., & Hopp, U. 1998, *ApJ*, 493, L23
- Searle, L., Sargent, W. L. W., & Bagnuolo, W. G. 1973, *ApJ*, 179, 427
- Skillman, E., & Kennicutt, R. C., Jr. 1993, *ApJ*, 411, 655
- Stasińska, G. 1990, *A&AS*, 83, 501
- Tantalo, R., Chiosi, C., Bressan, A., & Fagotto, F. 1996, *A&A*, 311, 361
- Telles, E., & Terlevich, R. 1997, *MNRAS*, 286, 183
- Thuan, T. X. 1985, *ApJ*, 299, 881
- Thuan, T. X., & Izotov, Y. I. 1997, *ApJ*, 489, 623
- Thuan, T. X., Izotov, Y. I., & Lipovetsky, V. A. 1995, *ApJ*, 445, 108 (TIL95)
- . 1996, *ApJ*, 463, 120
- . 1997, *ApJ*, 477, 661
- Thuan, T. X., Lipovetsky, V. A., Martin, J.-M., & Pustilnik, S. A. 1999a, *A&AS*, in press
- Thuan, T. X., Sauvage, M., & Madden, S. 1999b, *ApJ*, 516, 783
- Tomkin, J., Lemke, M., Lambert, D. L., & Sneden, C. 1992, *AJ*, 104, 1568
- van Zee, L., Westpfahl, D., Haynes, M.P., & Salzer, J.J. 1998, *AJ*, 115, 1000
- Viallefond, F. & Thuan, T.X. 1983, *ApJ*, 269, 444
- Walsh, J. R., & Roy, J.-R. 1987, *ApJ*, 319, L57
- . 1989, *MNRAS*, 239, 297
- Weaver, T. A., & Woosley, S. E. 1993, *Phys. Rep.*, 227, 65
- Whitford, A. E. 1958, *AJ*, 63, 201
- Woosley, S. E., & Weaver, T. A. 1995, *ApJS*, 101, 181

Fig. 1.— MMT spectrum of SBS 1415+437 within a $1''.5 \times 5''$ aperture with nebular emission line identifications.

Fig. 2.— *HST* FOS spectrum of SBS 1415+437 within a $0''.86$ round aperture with nebular emission line identifications. The Si III] $\lambda 1892$ emission line is not present in the UV spectrum. Instead an absorption feature is seen.

Fig. 3.— (a) The C/O abundance ratio vs. oxygen abundance for a sample of metal-deficient blue compact galaxies (open circles, Izotov & Thuan 1999). The filled circle represents SBS 1415+437. The solar value is shown by the symbol \odot ; (b) Si/O abundance ratio vs. oxygen abundance. The symbols have the same meaning as in Fig. 3a.

Fig. 4.— Spatial distribution of the electron temperature $T_e(\text{O III})$, oxygen abundance and heavy element-to-oxygen abundance ratios. The origin is taken to be at the brightest H II region. At the distance $D = 11.4$ Mpc of SBS 1415+437, $1''$ is equivalent to 55 pc.

Fig. 5.— *HST* WFPC2 I image of the comet-like galaxy SBS 1415+437 with a bright supergiant H II region at its SW side and unresolved diffuse stellar emission and resolved stars along the body of the galaxy.

Fig. 6.— Magnified I image of the brightest H II region in SBS 1415+437. There is a chain of bright stars along the NE - SW direction implying propagating star formation.

Fig. 7.— *HST* $(V - I)$ image of SBS 1415+437. Blue $(V - I)$ colors are dark and red $(V - I)$ colors are light. There are three blue H II regions at the SW end of the galaxy and two fainter H II regions in its central part. The brightest H II region has a filamentary structure and shows supernova superbubbles with dust patches mixed in. Resolved red stars can be seen in the main body of the galaxy.

Fig. 8.— Magnified $(V - I)$ image of the brightest H II region. Blue $(V - I)$ colors are dark and red $(V - I)$ colors are light. The white points to the NE are resolved red stars. There is a clear age difference for the two stellar clusters to the SW. The southernmost cluster contains only hot O stars and is younger while red supergiant stars are present in the older cluster to the north.

Fig. 9.— $(V - I)$ color vs. distance for stars in the brightest H II region. There is a clear color gradient, implying a systematic age gradient from the NE to the SW and propagating star formation.

Fig. 10.— Spatial distribution of the ionized gas velocity as derived from the $\text{H}\alpha$ (filled circles) and $[\text{O III}] \lambda 5007$ (open circles) emission lines. The origin is placed on the brightest H II region. The linear regression fit to the data points is shown by the solid line.

Fig. 11.— (a) V (open circles) and I (filled circles) surface brightness distributions as a function of the equivalent radius. The exponential fits are shown by solid lines; (b) $(V - I)$ color distribution as a function of the equivalent radius. The blue colors at $r \lesssim 5''$ are associated with the star-forming region. The diffuse low-intensity extended component has a nearly constant color.

Fig. 12.— The distribution of errors with magnitude as determined by DAOPHOT for (a) V and (b) I photometry.

Fig. 13.— Labeling of the 6 different regions in SBS 1415+437 selected for stellar population color - magnitude diagram analysis.

Fig. 14.— Color - magnitude diagrams of stellar populations in the regions of SBS 1415+437 defined in Figure 13. The isochrones (solid lines) are from Bertelli et al. (1994) and are labelled by the logarithm of age in yr. Dashed lines represent the region of 1 Gyr asymptotic giant branch stars. Dotted lines show the extinction-corrected observational limits corresponding to V and I equal to 28 mag. There is a gradual age increase from region I to region VI, implying propagating star formation from the NE (region VI) to the SW (region I). The typical photometric errors are shown in Fig. 14a.

Fig. 15.— MMT spectra of regions III to VI. The spectral energy distributions show blue colors indicative of young stellar populations.

Fig. 16.— (a) Extinction-corrected spectrum of region III (thin solid line) on which is superposed the theoretical stellar + gaseous spectral energy distribution (SED) of a stellar population with age 4.7 Myr (thick solid line). The stellar energy distribution is taken from Schaerer & Vacca (1998) and the gaseous

continuum is calculated using the observed equivalent width of $H\beta$ and electron temperature $T_e(\text{O III})$. (b) Decomposition of the theoretical stellar + gaseous spectral energy distribution in Fig. 16a (thick solid line) into stellar and gaseous emission. The relative contribution of the gaseous emission increases toward the red part of the spectrum. The emission line fluxes are taken from the observations.

Fig. 17.— (a) Uncorrected for extinction spectrum of region V on which are superposed the theoretical energy distributions of stellar populations with ages $\log t = 7.5, 8.0$ and 8.1 . The strong change in spectral energy distributions (SED) between $\log t = 8.0$ and $\log t = 8.1$ is caused by the appearance of the first asymptotic giant branch stars in the latter case. The theoretical SEDs are calculated using isochrones from Bertelli et al. (1994) and the stellar atmosphere model compilation from Lejeune et al. (1998), for a metallicity equal to $1/20$ that of the Sun. A Salpeter IMF and a lower stellar mass limit of $0.6 M_\odot$ have been adopted. The best fit is achieved with a theoretical SED with age $\log t = 8.1$; (b) Extinction-corrected spectrum of region V on which are superposed theoretical SEDs. The best fit is a SED with $\log t$ between 7.2 and 8.0 .

TABLE 1
OBSERVATIONAL CHARACTERISTICS OF SBS 1415+437

Parameter	Value
$\alpha(2000)$	$14^h 17^m 01^s.3$
$\delta(2000)$	$+43^\circ 12' 26''$
l^I, b^I	$84^\circ, 66^\circ$
d_{25}^a	$46''$
D (Mpc) ^b	11.4
d (kpc) ^a	2.53
V^a	15.55 ± 0.01
$V - I^a$	0.07 ± 0.01
M_B	-14.68
μ_V (mag arcsec ⁻²) ^a	21.00 ± 0.04
μ_I (mag arcsec ⁻²) ^a	20.69 ± 0.03
α^{-1} (kpc) ^a	0.27
v_{opt} (km s ⁻¹) ^a	607 ± 12
v_{HI} (km s ⁻¹) ^c	607 ± 2
Δv_{20} (km s ⁻¹) ^c	74 ± 5
Δv_{50} (km s ⁻¹) ^c	53 ± 3
F_{HI} ($10^6 M_\odot \text{ Mpc}^{-2}$) ^c	1.14 ± 0.08
M_{HI} ($10^8 M_\odot$) ^c	1.48
L_B ($10^8 L_{B\odot}$) ^d	1.16
M_{HI}/L_B ($M_\odot/L_{B\odot}$)	1.3

^afrom this paper. The diameter d_{25} is derived from Figure 11, adopting a minor-to-major axis ratio of 0.12. V and I magnitudes are derived by integrating the surface brightness profiles from 0 to an equivalent radius of $16''$.

^b redshift distance corresponding to $H_0 = 75 \text{ km s}^{-1} \text{ Mpc}^{-1}$ and a systematic velocity of 607 km s^{-1} , corrected to the Local Group velocity centroid. The Virgo-centric flow model described by Kraan-Korteweg (1986) with a Virgo-centric infall motion of 220 km s^{-1} has been adopted.

^cH I measurements obtained with the Nançay radio telescope by Thuan et al. (1999a).

^d Adopting $M_B(\text{sun}) = 5.48 \text{ mag}$.

TABLE 2
EMISSION LINE INTENSITIES

Ion	MMT					
	1''5×5'' aperture		1''5×0''6 aperture		HST	
	$F(\lambda)/F(\text{H}\beta)$	$I(\lambda)/I(\text{H}\beta)$	$F(\lambda)/F(\text{H}\beta)$	$I(\lambda)/I(\text{H}\beta)$	$F(\lambda)/F(\text{H}\beta)$	$I(\lambda)/I(\text{H}\beta)$
1883 Si III]	0.211±0.030	0.228±0.033
1907 C III]	0.467±0.045	0.506±0.048
3727 [O II]	0.973±0.014	1.054±0.017	0.838±0.013	0.832±0.015	0.695±0.046	0.675±0.049
3750 H12	0.022±0.001	0.034±0.003
3770 H11	0.026±0.001	0.038±0.003	0.018±0.002	0.064±0.010
3798 H10	0.039±0.002	0.052±0.003	0.034±0.002	0.080±0.006
3835 H9	0.051±0.002	0.065±0.003	0.043±0.003	0.089±0.006
3868 [Ne III]	0.275±0.005	0.294±0.005	0.274±0.005	0.271±0.005	0.308±0.030	0.298±0.031
3889 He I + H8	0.168±0.003	0.188±0.004	0.164±0.004	0.206±0.005	0.185±0.032	0.243±0.052
3968 [Ne III] + H7	0.229±0.004	0.252±0.005	0.216±0.004	0.255±0.006	0.245±0.031	0.305±0.050
4026 He I	0.013±0.002	0.014±0.002	0.014±0.003	0.014±0.003
4101 H δ	0.245±0.004	0.265±0.005	0.230±0.005	0.266±0.006	0.230±0.030	0.290±0.049
4340 H γ	0.453±0.007	0.474±0.008	0.442±0.007	0.467±0.008	0.416±0.039	0.460±0.052
4363 [O III]	0.086±0.002	0.088±0.002	0.089±0.003	0.087±0.003	0.094±0.027	0.091±0.027
4471 He I	0.033±0.001	0.034±0.001	0.032±0.002	0.031±0.002
4658 [Fe III]	0.008±0.001	0.008±0.001	0.006±0.002	0.006±0.002
4686 He II	0.025±0.001	0.025±0.001	0.028±0.002	0.027±0.002
4713 [Ar IV] + He I	0.011±0.001	0.011±0.001	0.011±0.002	0.011±0.002
4740 [Ar IV]	0.005±0.001	0.005±0.001	0.005±0.002	0.005±0.002
4861 H β	1.000±0.015	1.000±0.015	1.000±0.016	1.000±0.016	1.000±0.061	1.000±0.066
4921 He I	0.009±0.001	0.009±0.001	0.008±0.002	0.008±0.002
4959 [O III]	1.198±0.018	1.184±0.018	1.249±0.019	1.216±0.019	1.263±0.072	1.207±0.072
5007 [O III]	3.574±0.052	3.523±0.052	3.771±0.057	3.670±0.056	3.720±0.178	3.554±0.178
5876 He I	0.103±0.002	0.096±0.002	0.101±0.002	0.097±0.002	0.105±0.025	0.100±0.025
6300 [O I]	0.023±0.001	0.021±0.001	0.019±0.001	0.019±0.001
6312 [S III]	0.014±0.001	0.013±0.001	0.014±0.001	0.013±0.001
6363 [O I]	0.008±0.001	0.007±0.001	0.005±0.001	0.005±0.001
6563 H α	3.053±0.044	2.773±0.044	2.888±0.043	2.773±0.046	2.917±0.142	2.767±0.154
6583 [N II]	0.041±0.001	0.037±0.001	0.030±0.002	0.029±0.002
6678 He I	0.031±0.001	0.028±0.001	0.030±0.001	0.029±0.001
6717 [S II]	0.097±0.002	0.087±0.002	0.075±0.002	0.072±0.002
6731 [S II]	0.072±0.002	0.065±0.001	0.053±0.002	0.051±0.002
7065 He I	0.028±0.001	0.025±0.001	0.025±0.001	0.024±0.001
7135 [Ar III]	0.044±0.001	0.039±0.001	0.041±0.001	0.039±0.001
$C(\text{H}\beta)$ dex	0.120±0.020		0.025±0.019		0.020±0.060	
$F(\text{H}\beta)^a$	7.36±0.02		0.94±0.01		0.64±0.03	
$EW(\text{H}\beta)$ Å	159±1		140±1		101±4	
$EW(\text{abs})$ Å	0.8±0.1		3.6±0.2		4.6±1.8	

^ain units of 10^{-14} ergs s⁻¹cm⁻².

TABLE 3
HEAVY ELEMENT ABUNDANCES

Property	MMT		<i>HST</i> ^a
	1''5×5'' aperture	1''5×0''6 aperture	
$T_e(\text{O III})(\text{K})$	17,000±220	16,600±270	17,100±2,700
$T_e(\text{O II})(\text{K})$	14,600±180	14,500±220	14,700±2,200
$T_e(\text{S III})(\text{K})$	15,800±190	15,400±220	15,900±2,200
$N_e(\text{S II})(\text{cm}^{-3})$	80±40	10±10	10±10
$\text{O}^+/\text{H}^+(\times 10^5)$	0.99 ± 0.04	0.81 ± 0.04	0.62 ± 0.25
$\text{O}^{++}/\text{H}^+(\times 10^5)$	2.87 ± 0.10	3.15 ± 0.13	2.86 ± 1.08
$\text{O}^{+3}/\text{H}^+(\times 10^5)$	0.11 ± 0.01	0.11 ± 0.01	...
$\text{O}/\text{H}(\times 10^5)$	3.96 ± 0.10	4.07 ± 0.14	3.48 ± 1.11
12 + log(O/H)	7.60 ± 0.01	7.61 ± 0.01	7.54 ± 0.14
$\text{C}^{++}/\text{O}^{++}$	0.16 ± 0.03
ICF(C)	1.05
log(C/O)	-0.78 ± 0.10
$\text{N}^+/\text{H}^+(\times 10^7)$	2.86 ± 0.11	2.28 ± 0.10	...
ICF(N)	3.99	5.05	...
log(N/O)	-1.54 ± 0.03	-1.55 ± 0.03	...
$\text{Ne}^{++}/\text{H}^+(\times 10^5)$	0.51 ± 0.02	0.50 ± 0.02	0.51 ± 0.20
ICF(Ne)	1.38	1.29	1.22
log(Ne/O)	-0.75 ± 0.02	-0.80 ± 0.03	-0.75 ± 0.26
$\text{Si}^{++}/\text{C}^{++}$	0.16 ± 0.02
ICF(Si)	1.33
log(Si/C)	-0.68 ± 0.09
log(Si/O)	-1.46 ± 0.27
$\text{S}^+/\text{H}^+(\times 10^7)$	1.58 ± 0.04	1.29 ± 0.04	...
$\text{S}^{++}/\text{H}^+(\times 10^7)$	5.63 ± 0.36	6.08 ± 0.59	...
ICF(S)	1.44	1.60	...
log(S/O)	-1.58 ± 0.02	-1.54 ± 0.03	...
$\text{Ar}^{++}/\text{H}^+(\times 10^7)$	1.30 ± 0.04	1.33 ± 0.05	...
$\text{Ar}^{+3}/\text{H}^+(\times 10^7)$	0.57 ± 0.13	0.58 ± 0.21	...
ICF(Ar)	1.06	1.04	...
log(Ar/O)	-2.30 ± 0.03	-2.31 ± 0.05	...
$\text{Fe}^{++}/\text{H}^+(\times 10^7)$	1.63 ± 0.24	1.23 ± 0.49	...
ICF(Fe)	4.99	6.32	...
log(Fe/O)	-1.69 ± 0.03	-1.61 ± 0.07	...
[O/Fe]	0.27 ± 0.03	0.30 ± 0.07	...

^aThe electron temperature $T_e(\text{O III})$ from the MMT spectrum within the 1''5×0''6 aperture is adopted in deriving C and Si abundances.

TABLE 4
HELIUM ABUNDANCE

Property	1''5×5'' aperture	1''5×0''6 aperture
$T_e(\text{He}^+)$	17,000	16,600
$N_e(\text{He}^+)$	10	10
$\tau(\lambda 3889)$	0.1	0.1
$\gamma(\lambda 4471)$	0.002	0.002
$\text{He}^+/\text{H}^+(\lambda 4471)$	0.073±0.003	0.067±0.004
$\gamma(\lambda 5876)$	0.004	0.004
$\text{He}^+/\text{H}^+(\lambda 5876)$	0.080±0.002	0.080±0.002
$\gamma(\lambda 6678)$	0.001	0.001
$\text{He}^+/\text{H}^+(\lambda 6678)$	0.083±0.003	0.085±0.004
$\text{He}^+/\text{H}^+(\text{weighted mean})$	0.079±0.001	0.079±0.002
$\text{He}^{++}/\text{H}^+(\times 10^2)$	0.23 ± 0.01	0.25 ± 0.02
ICF(He)	1.000	1.000
$\text{He}/\text{H}(\text{weighted mean})$	0.082±0.001	0.081±0.002
$Y(\text{weighted mean})$	0.246±0.004	0.245±0.005

TABLE 5
COMPLETENESS OF THE POINT-LIKE SOURCES PHOTOMETRY

Magnitude range	F569W	F791W
20 – 21	100	100
21 – 22	100	100
22 – 23	100	100
23 – 24	92±10	88±11
24 – 25	83±12	70± 6
25 – 26	59±12	35± 8
26 – 27	22±10	4± 2

TABLE 6
PHOTOMETRIC PROPERTIES OF REGION III

Property	Model ^a	Observations
$U - B$	-0.76	...
$B - V$	0.16	...
$V - R$	0.18	...
$V - I$	-0.06	-0.07 ^b
$V - K$	0.36	...

^aFor a stellar population with age $t=4.7$ Myr.

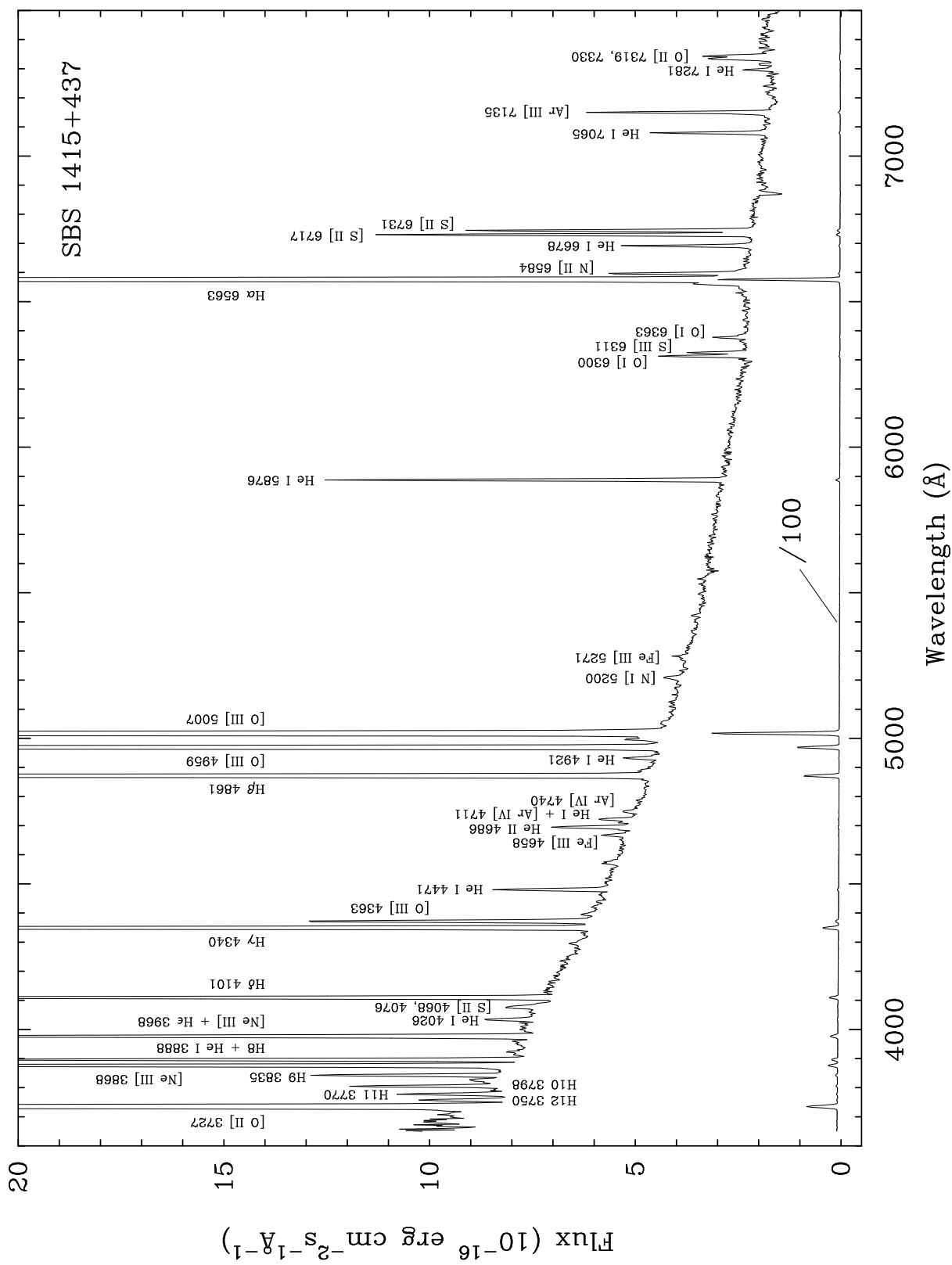
^bNot corrected for extinction. ($V - I$) = -0.16 mag ($C(\text{H}\beta) = 0.12$, $A_V = 0.25$ mag, Table 2) after correction for interstellar extinction.

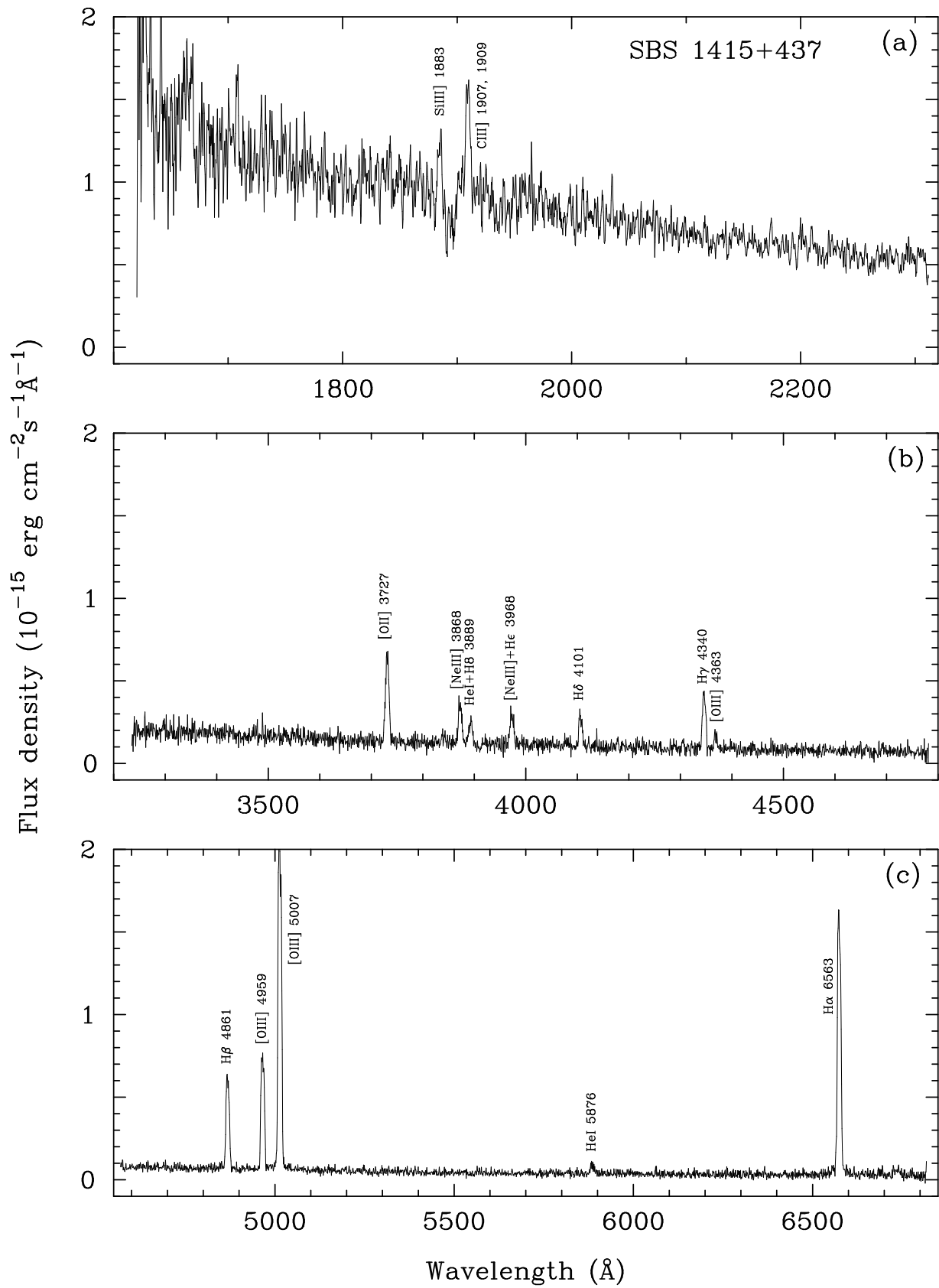
TABLE 7
PHOTOMETRIC PROPERTIES OF REGION V

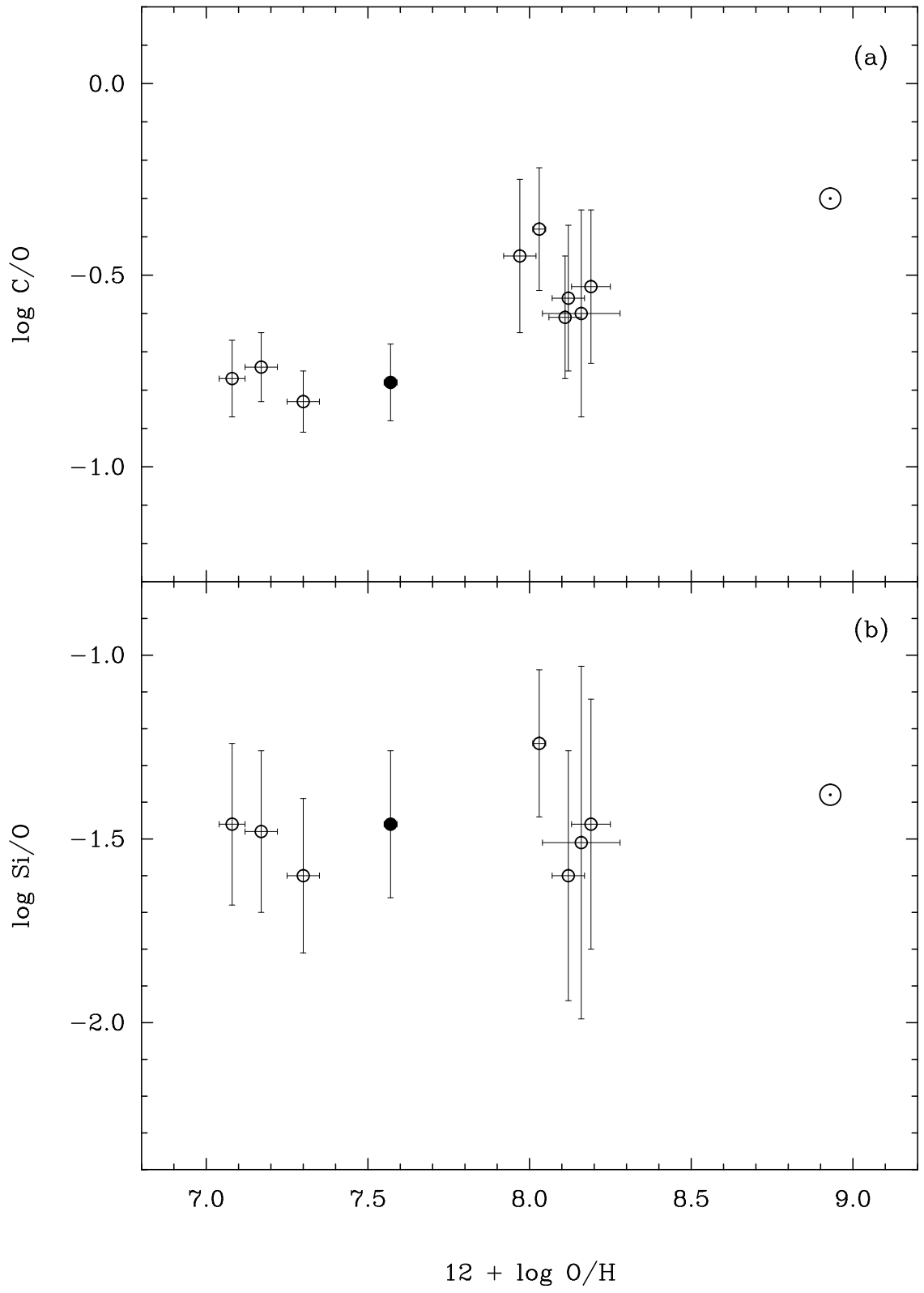
Property	Model						Observations
	7.2 ^a	7.3 ^a	7.4 ^a	7.5 ^a	8.0 ^a	8.1 ^a	
$U - B$	-0.93	-0.87	-0.84	-0.72	-0.48	-0.40	...
$B - V$	-0.04	0.00	0.00	0.01	0.08	0.20	...
$V - R$	0.21	0.25	0.24	0.22	0.26	0.43	...
$V - I$	0.21	0.31	0.29	0.35	0.43	0.79	0.40 ^b
$V - K$	0.54	0.76	0.68	0.74	0.83	1.60	...

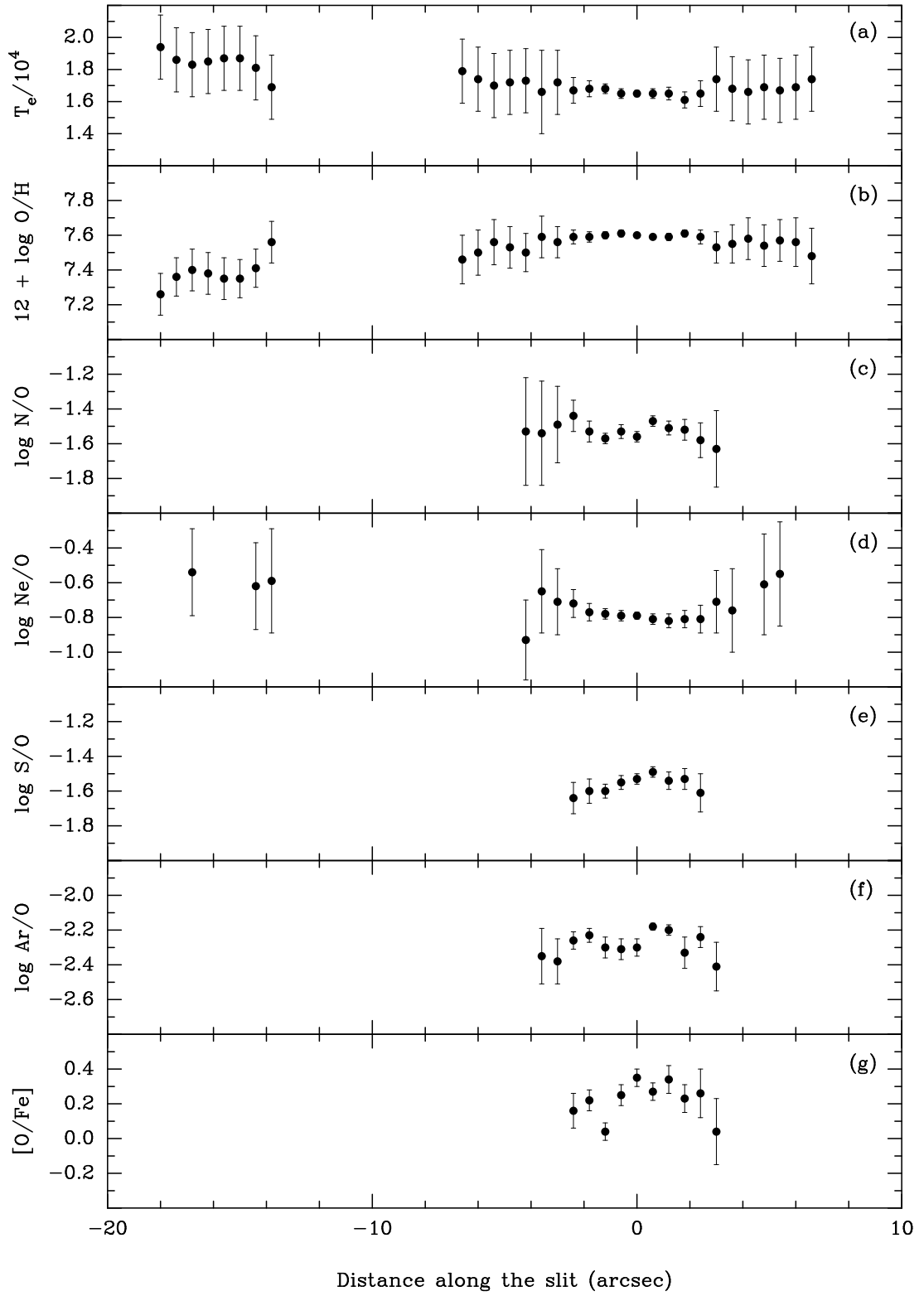
^a $\log t$, where t is the age in yr.

^bNot corrected for extinction. ($V - I$) = 0.25 mag after correction for interstellar extinction ($C(\text{H}\beta) = 0.26$, $A_V = 0.55$ mag).









This figure "fig5.jpg" is available in "jpg" format from:

<http://arxiv.org/ps/astro-ph/9905345v1>

This figure "fig6.jpg" is available in "jpg" format from:

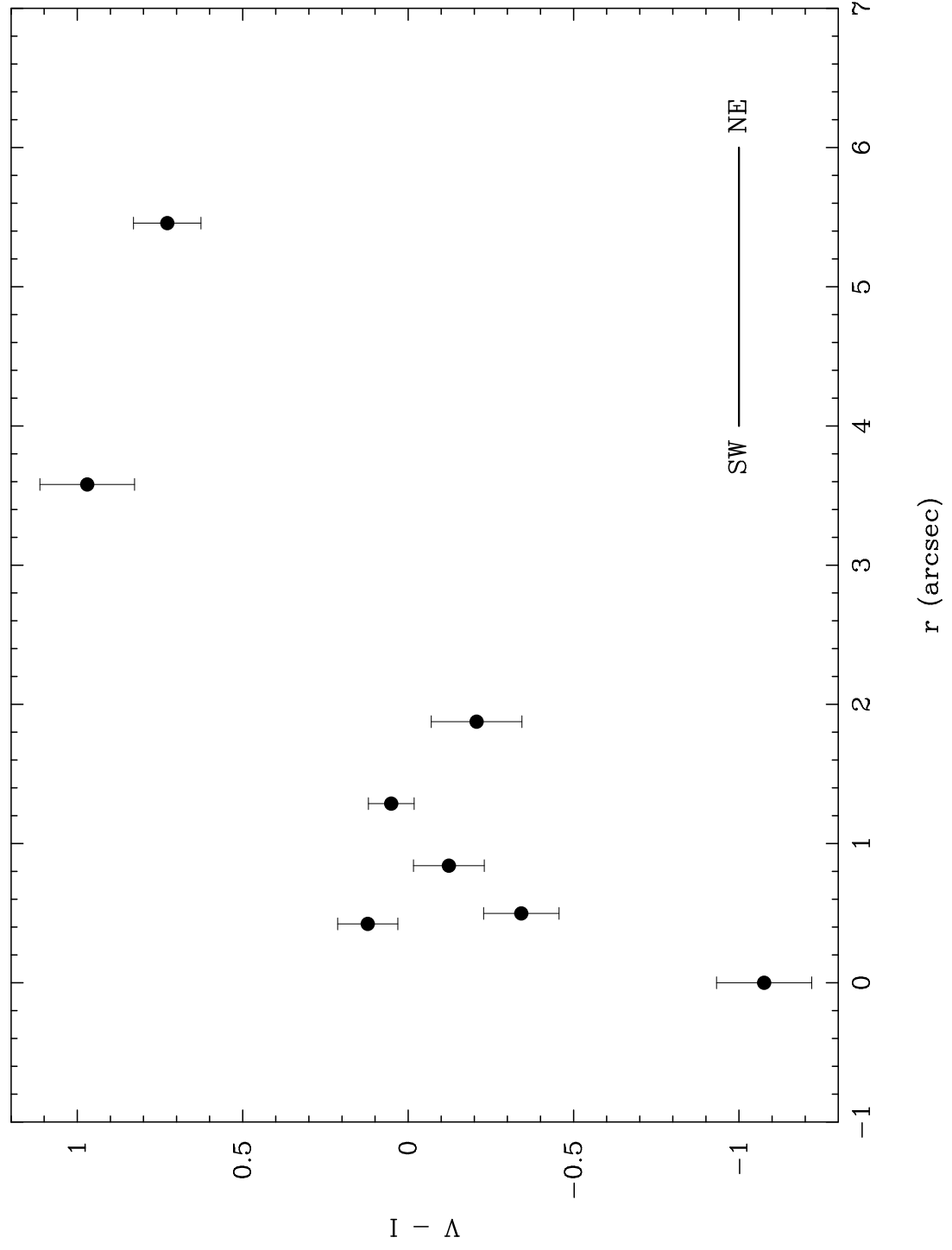
<http://arxiv.org/ps/astro-ph/9905345v1>

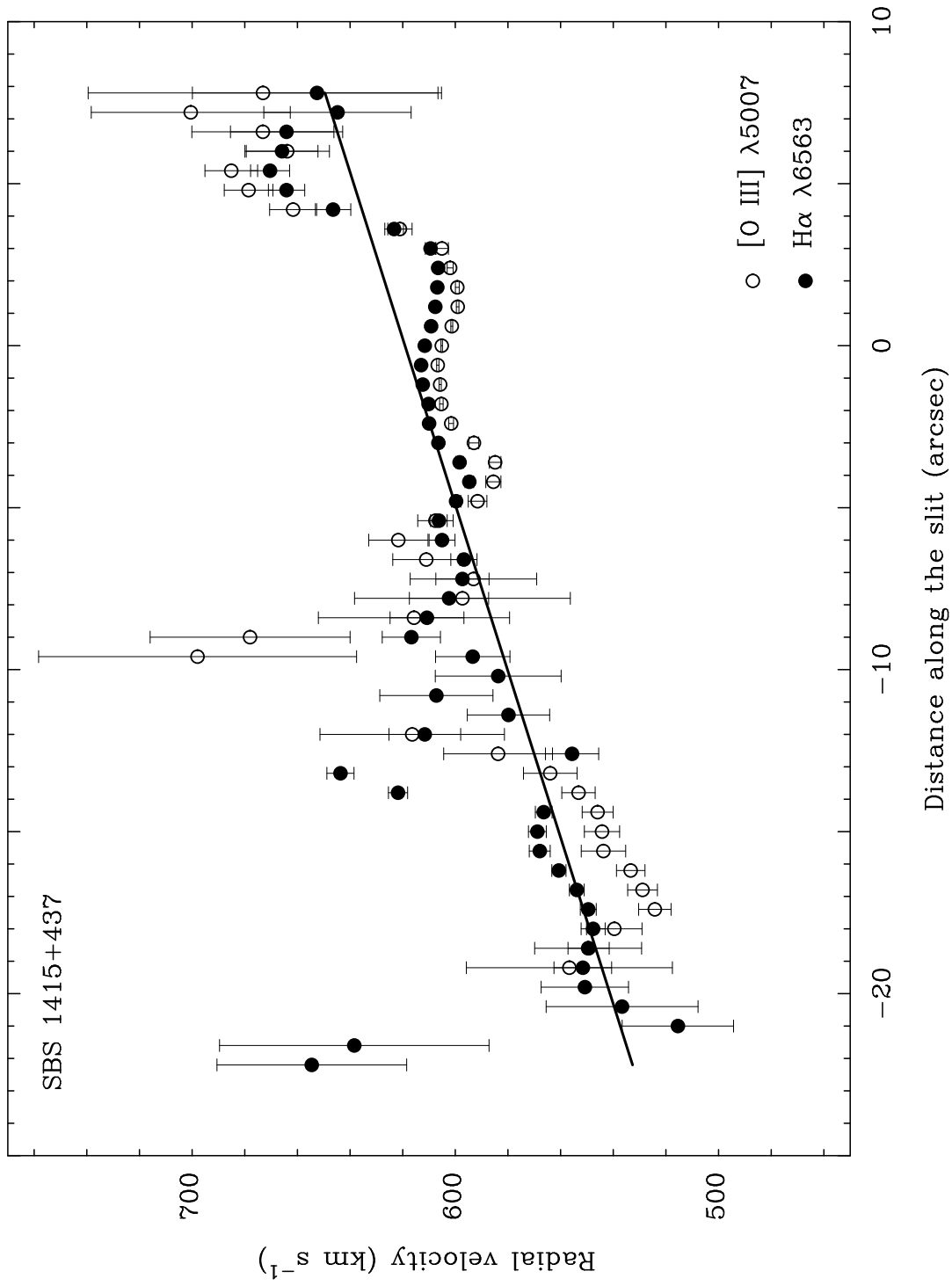
This figure "fig7.jpg" is available in "jpg" format from:

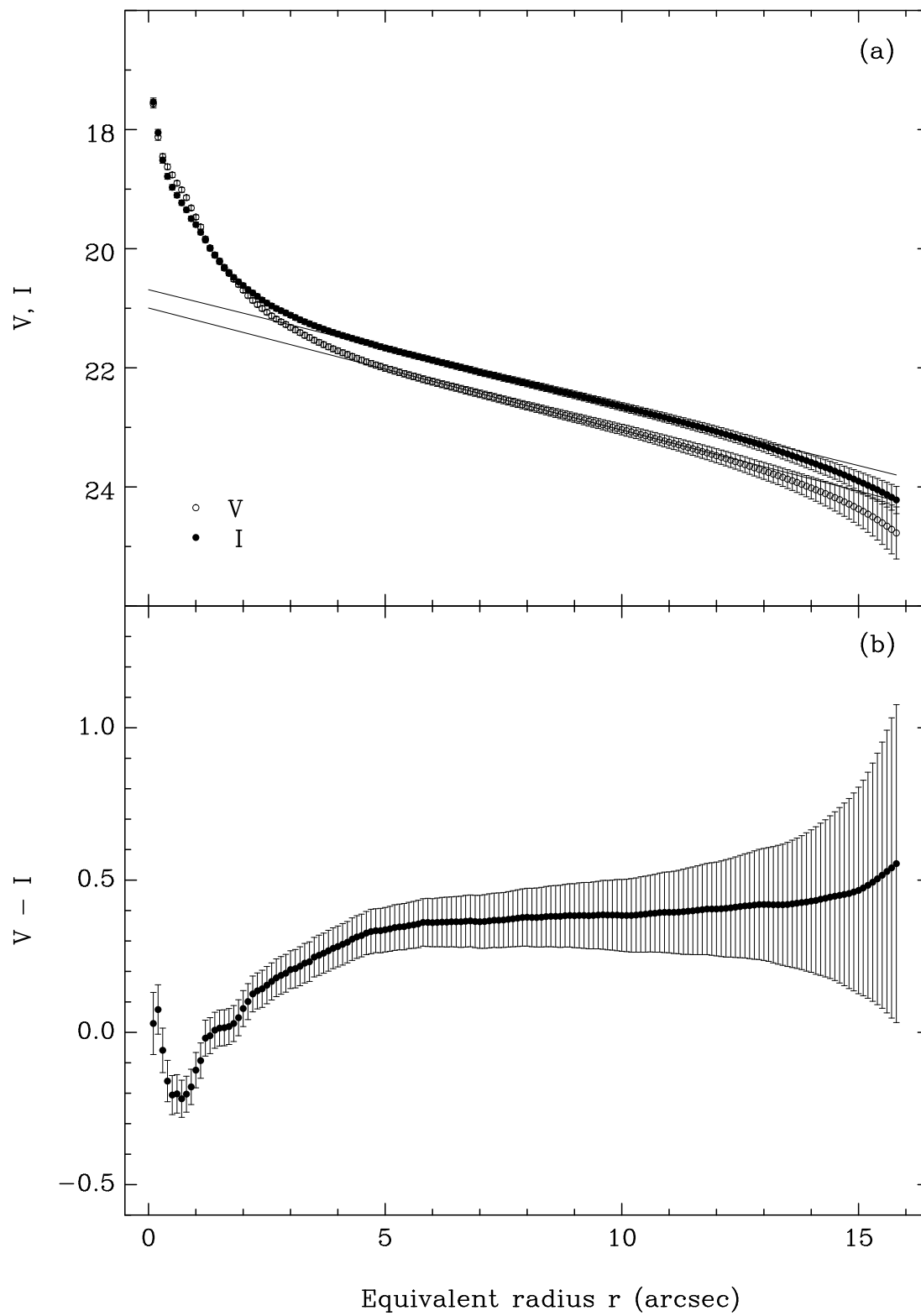
<http://arxiv.org/ps/astro-ph/9905345v1>

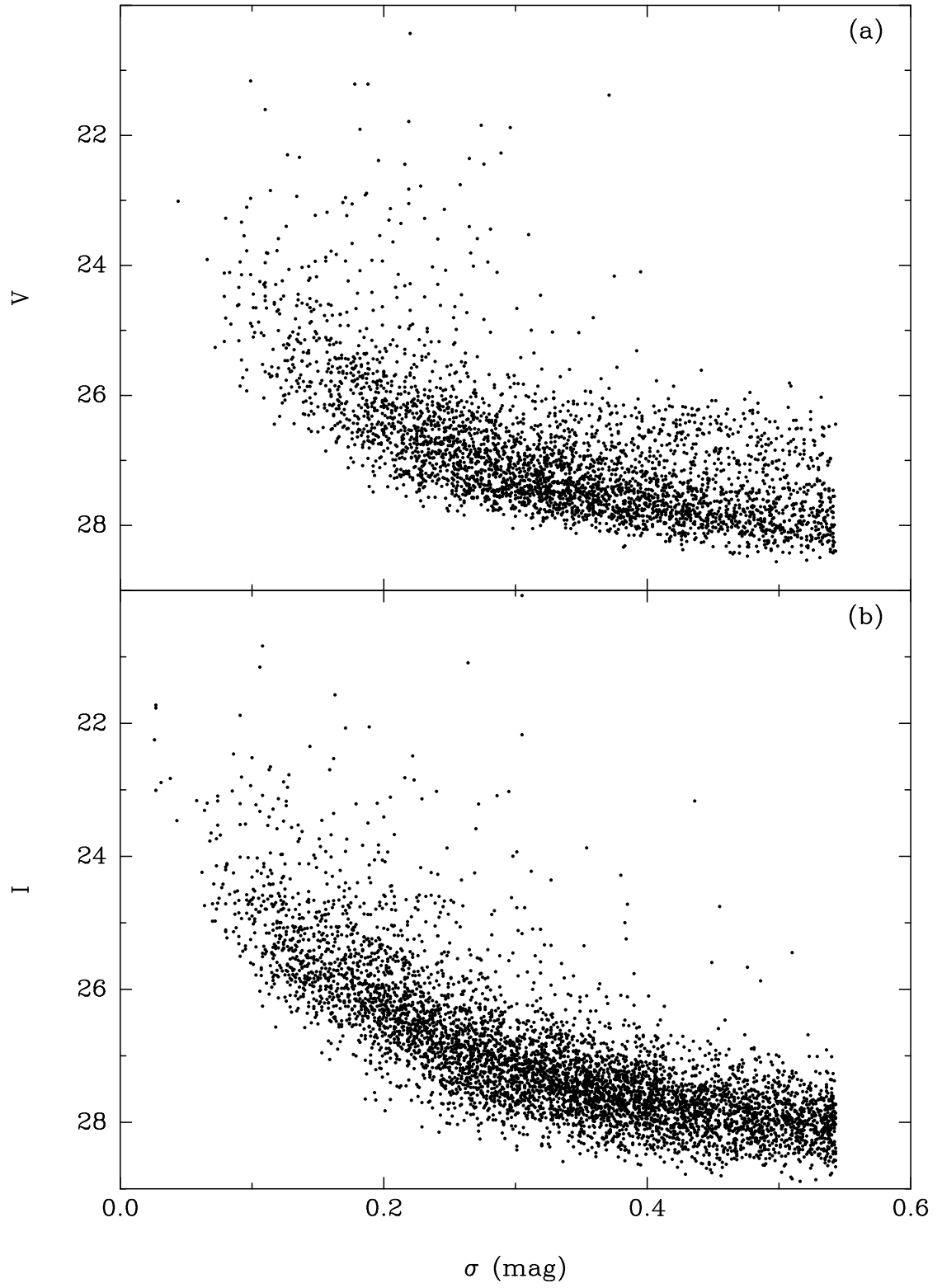
This figure "fig8.jpg" is available in "jpg" format from:

<http://arxiv.org/ps/astro-ph/9905345v1>



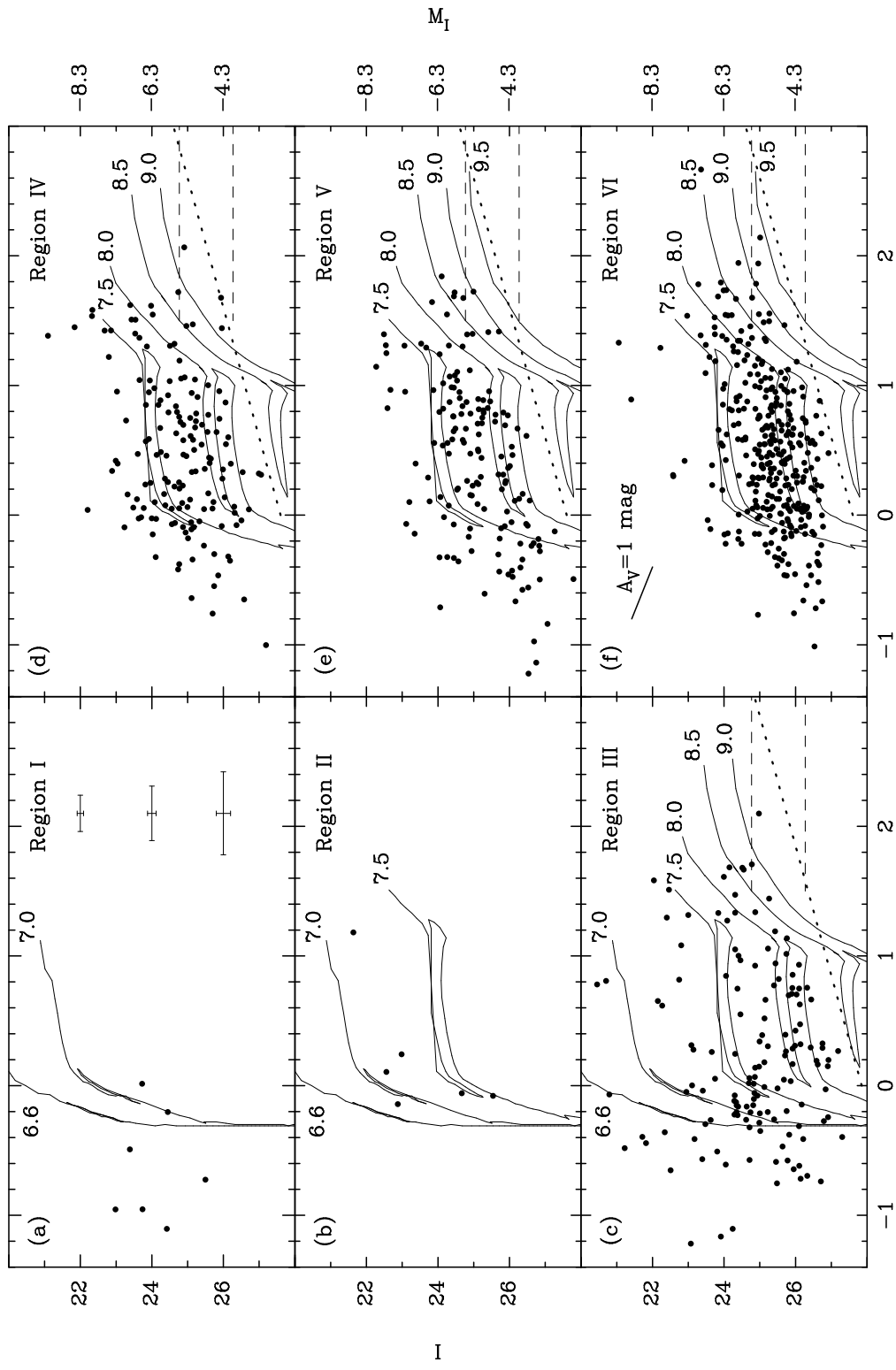






This figure "fig13.jpg" is available in "jpg" format from:

<http://arxiv.org/ps/astro-ph/9905345v1>



V - I

